Wirelessly operated bioelectronic sutures for the monitoring of deep surgical wounds

Viveka Kalidasan[1,&,*], Xin Yang[1,&], Ze Xiong[1,2,3,&,*], Renee R. Li[4,5], Haicheng Yao[6], Hareesh Godaba[6], Sybil Obuobi[7,‡], Priti Singh[8], Xin Guan[6], Xi Tian[1], Selman A. Kurt[1], Zhipeng Li[1], Devika Mukherjee[7], Ravisankar Rajarethinam[9], Choon Seng Chong[10], Jiong-Wei Wang[4,5,11], Pui Lai Rachel Ee[7], Weiqiang Loke[8], Benjamin C. K. Tee[6,2,3], Jianyong Ouyang[6], Christopher J. Charles[4,5,12], John S. Ho[1,2,3,*]

[1]Department of Electrical and Computer Engineering, National University of Singapore, Singapore
[2]Institute for Health Innovation and Technology, National University of Singapore, Singapore
[3]The N.1 Institute for Health, National University of Singapore, Singapore
[4]Cardiovascular Research Institute, National University Heart Centre, Singapore
[5]Department of Surgery, Yong Loo Lin School of Medicine, National University of Singapore, Singapore
[6]Department of Materials Science and Engineering, National University of Singapore, Singapore
[7]Department of Pharmacy, National University of Singapore, Singapore
[8]Faculty of Dentistry, National University of Singapore, Singapore
[9]Institute of Molecular and Cell Biology, Agency for Science, Technology and Research, Singapore
[10]Department of Surgery, National University Hospital, Singapore
[11]Department of Physiology, Yong Loo Lin School of Medicine, National University of Singapore, Singapore
[12]Christchurch Heart Institute, Department of Medicine, University of Otago, Christchurch, New Zealand
[‡]Present address: Drug Transport and Delivery Research Group, Department of Pharmacy, Faculty of Health Sciences, UiT-The Arctic University of Norway, N-9037, Tromsø, Norway.

[&]These authors contributed equally
*Corresponding authors, viveka_k@nus.edu.sg; elexio@nus.edu.sg; johnho@nus.edu.sg

Monitoring surgical wounds post-operatively is necessary to prevent infection, dehiscence and other complications. However, the monitoring of deep surgical sites is typically limited to indirect observations or to costly radiological investigations that often fail to detect complications before they become severe. Bioelectronic sensors could provide accurate and continuous monitoring from within the body, but the form factors of existing devices are not amenable to integration with sensitive wound tissues and to wireless data transmission. Here, we show that multifilament surgical sutures functionalized with a conductive polymer and incorporating pledgets with capacitive sensors operated via radiofrequency identification can be used to monitor physicochemical states of deep surgical sites. We show in live pigs that the sutures can monitor wound integrity, gastric leakage and tissue micromotions, and in rodents that the healing outcomes are equivalent to those of medical-grade sutures. Battery-free wirelessly operated bioelectronic sutures may facilitate post-surgical monitoring in a wide range of interventions.

The ability to monitor deep surgical wounds during patient recovery is a major and as yet unmet clinical need. Most surgical adverse events occur during post-operative management rather than during operation. Complications arising from the surgical wound – such as bleeding, dehiscence, leakage, and infection – represent the most frequent potentially preventable consequence of these events[1]. However, timely detection of complications remains challenging across many classes of interventions because they manifest deep within the body. Current clinical approaches to detect deep complications primarily rely on external signs such as body temperature, respiratory patterns, and skin color[2,3]. These indicators do not directly reflect the physiochemical and microbial environment of the surgical wound. Critically, they often do not present until complications become severe[4]. Although radiological investigations using ultrasound, computed tomography, or contrast enema can provide accurate evaluation, they are costly and require specialized training to perform. Furthermore, these methods do not address the need to monitor the surgical site after patient discharge from the hospital, where substantial risk of adverse events remains[5,6].

Bioelectronic sensors provide the opportunity to monitor physiological parameters directly from within the body. While a wide variety of implantable sensors have been developed for both basic research and clinical applications, existing devices have form factors that limit their integration with sensitive and deeply-situated tissues. For example, current devices used for clinical monitoring within blood vessels[7] and the gastrointestinal tract[8,9] are based on rigid, centimeter-sized capsules, thereby posing risk of injury to the surgical wound. Flexible, stretchable electronics can overcome the mechanical mismatch with soft tissues[10-16]. However, interfacing such devices within deep tissues thus far requires additional surgical steps for fixation[17] and relatively large components for wireless data transmission[18].

In contrast, surgical sutures provide a promising approach to monitor surgical wounds owing to their wide clinical use and intimate integration with wound tissues. Recent developments in materials and fabrication

have enabled a variety of sensing sutures that can detect relevant physiological parameters while integrating with wound tissues to promote healing. Examples include electronic strips instrumented with thermal sensors and heaters[19], flexible conductive threads for biofluid extraction and analysis[20-23], and drug-eluting multilayered silk fibers integrated with temperature and strain sensors[24]. However, while these sutures can provide flexible mechanics and multiple sensing functionalities, their utility for monitoring deep surgical wounds is limited by the need for wired connections to external components for power supply and data acquisition (**Supplementary Table 1**). Separately, progress in integrated sensing systems have recently yielded a wide range of implantable wireless and battery-free devices for continuous sensing[25]. These solutions, however, generally have planar form factors that are incompatible with thread-like sutures because of requirements for wireless communication.

Here we report the design and demonstration of wireless sensing (WiSe) sutures capable of directly monitoring deep surgical wounds. WiSe sutures consist of medical-grade multifilament sutures, functionalized by a conductive polymer (PEDOT:PSS) that provides wireless responsivity while fully retaining the mechanical pliability of the underlying suture. The sutures are wirelessly operated using a custom radio-frequency identification technique in which a miniaturized electronic pledget attached to the suture generates harmonics of the incident signal for interference-free readout of physical and chemical sensors. We demonstrate the utility of the WiSe sutures in monitoring wound integrity, leakage of gastric fluid, and tissue micromotions at deep surgical sites *in vivo* in a porcine model. Chronic studies in rats over two weeks further show the long-term wireless performance and show that the healing outcomes are equivalent to the underlying medical-grade suture. Additional experiments suggest the applicability of the approach across a broad range of suture size and types, and its utility for detection of other post-operative complications, such as wound infection.

Design of the wireless sensing system

The wireless sensing system comprises three key components: (i) a medical-grade non-resorbable suture rendered responsive to radio-frequency fields by a conductive polymer coating; (ii) a battery-free electronic pledget containing a nonlinear circuit and capacitive sensor (**Supplementary Fig. 1**); and (iii) a custom radio-frequency system for transmission of 1-2 GHz wireless signals and reception of backscattered 2-4 GHz second harmonic signals (**Fig. 1a, Supplementary Note 1**). Surgical use of the WiSe sutures involves minimal modification of the standard stitching procedure for pledgeted sutures. During formation of a continuous surgical stitch, the insulating section of the suture is threaded through the electronic pledget and secured by applying medical silicone to the electrical contacts (**Fig. 1b**, **Supplementary Videos 1 and 2**). The electromagnetic response of the combined surgical stitch and electronic pledget is described by the equivalent circuit in **Fig. 1c**. Owing to its radio-frequency conductivity, the entire surgical stitch functions as a dipole antenna and responds to the incident wireless signal through wireless backscattering. In this process, the reflection of the received signal by the electrical load consisting of an inductor-capacitor (*LC*) circuit and a Schottky diode generates the backscattered signal. The *LC* circuit incorporates a capacitive sensor which converts physiological signals into shifts in the circuit's resonant frequency. Due to its nonlinearity, the Schottky diode generates harmonics of the incident wireless signal **(Supplementary Video 3, Supplementary Note 2)**. Since biological tissues do not exhibit nonlinearity at radio-frequencies, the harmonic signal detected by the external wireless system is attributable to only the WiSe suture and is free of interference from the physiological environment.

Wireless monitoring of the WiSe sutures uses harmonic backscattering techniques originally developed for radio-frequency identification[26-28]. The wireless system is capable of operating either in the frequency-resolved mode or time-resolved mode. In the frequency-resolved mode, the wireless system measures the harmonic backscattering spectrum as the input signal is varied from 1 to 2 GHz (**Supplementary Video 4**). The position of the resonant dip in the spectrum encodes the state of the capacitive sensor (**Fig. 1d**). This feature enables detection of a broad range of complications, including infection and leakage of gastric fluid, irrespective of variations in the wireless environment. In the time-resolved mode, the wireless system records the amplitude of the backscattered signal with a temporal resolution of about 40 ms (**Fig. 1e**). Periodic variations in the signal amplitude reveal small motions of tissue around the suture due to physiological processes such as respiration or heartbeat, while a large decrease in the average signal amplitude can indicate suture breakage due to the change in the electrical length of the stitch.

Suture functionalization and characterization

We selected poly(3,4-ethylenedioxythiophene)-poly(styrene sulfonate) (PEDOT:PSS) treated with dimethyl sulfoxide (DMSO) as the conductive polymer coating as it has the highest reported conductivity among

solution-processed polymers[29]. Its biocompatibility and biostability are also well-validated[30]. The optimized functionalization protocol involves surface treatment to remove the waxy calcium stearate coating and improve surface adhesion; multiple cycles of soaking in PEDOT:PSS solution and vacuum drying; and finally deposition of a thin dielectric layer (parylene-C) for electrical insulation (**Supplementary Fig. 2**, Methods). Non-resorbable, silk sutures (size-0) were selected as base medical-grade sutures owing to their ease of coating with the conductive polymer and wide surgical use[31,32]. Scanning electron microscopy shows conformal coating of the conductive polymer and the dielectric layer around the silk fibers (**Fig. 2a, Supplementary Fig. 3**). **Fig. 2b** shows uniform Joule heating of the functionalized suture when 30 V is applied across the two ends of the suture, verifying that the conductive polymer coating is consistent across the length of the suture. The protocol can be adapted to realize a wireless response in a broad range of multifilament sutures of varying sizes, including vicryl and cotton (**Supplementary Fig. 4**).

Material testing experiments demonstrate that the functionalized sutures exhibit mechanical properties that are comparable to medical-grade sutures. WiSe sutures have a tensile strength of 320 MPa at a strain of ~28%, which is higher than that of unmodified silk suture as well as cotton and polyester sutures, but lower than monofilament nylon and polyglycolic acid sutures (**Fig. 2c** and **Supplementary Fig. 5**). **Fig. 2d** shows the measured tissue drag force per unit the circumference when the sutures are pulled through synthetic skin. The functionalized sutures exhibit a slightly increased drag force of 460 N/m compared to the unmodified silk suture (330 N/m) but is comparable to the nylon suture (490 N/m) and is lower than the cotton suture (550 N/m). The drag force is within the range of the tested medical-grade sutures, which is required to be sufficiently large enough to prevent excessive sliding against sutured tissue but small enough to avoid tissue damage during stitching.

Cell viability experiments over 72 hours indicate that the biocompatibility of the functionalized sutures is equivalent to the unmodified silk sutures (**Fig. 2e**). Direct exposure of PEDOT:PSS to the cellular environment also does not result in increased cytotoxicity, which is consistent with prior biocompatibility tests[31]. Confocal fluorescent imaging further confirms that the cells incubated with the functionalized sutures and unmodified silk sutures display similar viability and did not result in any change in morphology compared to normal cells (**Supplementary Fig. 6**).

Electrical, mechanical, and immersion tests demonstrate the stability of the electrical conductivity of the sutures under simulated physiological conditions. The electrical resistance of a 10-cm length WiSe suture is ~1 kΩ and exhibits minimal variation (±1.2%) over 2500 cycles of mechanical bending (**Fig. 2f**). Forming a loop around a 1-mm radius rod results in <15% change in resistance, indicating that conductivity can be substantially maintained through surgical knots (**Fig. 2g**). Over 3 weeks of immersion in phosphate buffer saline solution (1×PBS) at 37 °C (**Fig. 2h**) to mimic physiological conditions, the resistance increases by less than 10%. This stability can be attributed to the encapsulation layer, since sutures not coated with parylene-C exhibit ~30% increase in resistance under the same conditions. These results show that WiSe sutures exhibit electrical conductivity sufficient for wireless responsivity while also having mechanical properties and biocompatibility comparable to that of medical-grade sutures.

Wireless system design and optimization

Wireless operation of the WiSe sutures is based on the radio-frequency system shown in **Fig. 3a**. A custom-designed planar dipole antenna provides transmission of wireless signals in the 1–2 GHz band and reception of its second harmonic in the 2–4 GHz band (**Supplementary Fig. 7**). The forward and backward signal paths are separated using a directional coupler, and multiple stages of filters achieve high suppression (>75 dB) of the intrinsic harmonics. The second harmonic signal is measured using a spectrum analyzer with a noise floor of -120 dBm.

Full-wave simulations using a computational model of the human torso establish the operating power range of the system (**Supplementary Fig. 8**). **Fig. 3b** shows the simulated electric field distribution for incident (f_0) and backscattered ($2f_0$) signals for a WiSe suture stitched on the stomach wall and the reader is placed close to the human body. Power dissipation occurs primarily near the surface of human body (**Supplementary Fig. 9a and b**). The specific absorption rate (SAR) at an input power of 1 W at 1 GHz has a peak value of 4 W/kg averaged over 10 g of tissue. This value is below the 10 W/kg threshold for safe electromagnetic wave absorption (**Supplementary Fig. 9c**)[33]. We operate system with a duty cycle of 10% such that the time-averaged transmit power is less than 1 W to ensure safety of wireless operation.

The wireless operation depends on the relative position between transmitter and receiver as well as the geometry of the surgical stitch (**Fig. 3a**). Electromagnetic simulations establish the operating region in the

parameter space of the depth of the surgical site *d* and the length of the suture pattern *L* for three representative surgical stitches (Lembert, lockstitch and Cushing types) embedded in muscle tissue. These simulations constitute a lower bound to the operating depth because muscle tissue has one of the highest radio-frequency losses across all types of tissues[34]. Provided that the surgical stitches are continuous, all three types of stitches support a uniform current distribution after excitation by a wireless signal at 1 GHz and are capable of radiating the second harmonic signal at 2 GHz (**Fig. 3c-e**). Sutures forming stitches with length greater than 10 mm support an operating depth of at least 30 mm, assuming a maximum received harmonic power of -100 dBm (**Fig. 3f-h**). Operating depths of up to 50 mm can be achieved for stitches with lengths between 15-25 mm due to resonance of the dipole antenna formed by the particular stitch. The depth can potentially be further extended by increasing the conductivity of the suture or the dynamic range of the wireless system (**Extended Data Fig. 1, Supplementary Note 3**). **Supplementary Fig. 10a-c** show the simulated harmonic backscattering spectrum of the wireless system in the frequency-resolved readout mode for sutures with *L* = 20 mm and *d* = 25 mm. The spectrum exhibits a clear dip corresponding to the resonant frequency of the *LC* circuit. The position of the dip varies with the capacitance of the sensor with a sensitivity greater than 1.6 GHz/pF, which is compatible with a wide range of sensor designs based on planar interdigitated capacitor structures[35-37].

We further experimentally characterized the depth and robustness of the wireless readout by measuring the harmonic backscattering spectrum of WiSe sutures through layered porcine tissues. In agreement with simulation results, all three types of stitches with length *L* = 20 mm yielded a harmonic backscattering signal above noise level of -120 dBm for tissue thicknesses up to 40 mm (**Fig. 3i-k, Supplementary Fig. 11**). To test the effect of suturing on nonplanar tissue surfaces, frequency-resolved wireless readout was performed while a Lembert-type stitch was subjected to in-plane and out-of-plane bending from 0° to 90°. The variation in the received power is less than 5 dB for all out-of-plane angles and for in-plane angles less than 60°. The position of the resonant dip remained constant for all bending types and angles, which indicates consistent readout of the electronic pledget (**Extended Data Fig. 2a-d**). We also characterized wireless readout of multiple stitches as the spacing between two sutures with different resonant frequencies is varied. Distinct resonant dips in the harmonic backscattering spectra can be measured as long as the two sutures maintain a separation distance of more than 20 mm (**Extended Data Fig. 2e-h**).

Wireless detection of post-surgical complications in porcine model

To demonstrate clinically relevant wireless detection of post-surgical complications, we deployed WiSe sutures with multiple attached sensors in a porcine model of a deep surgical wound. **Fig. 4a** shows the *in vivo* experimental setup in which the WiSe sutures were used to close a ~10 cm length incision made on the latissimus dorsi muscle. During suturing, two electronic pledgets (P1 and P2) with different resonant frequencies were attached. We adapted the pledgets to detect gastric leakage by functionalizing the surface of the interdigitated capacitor with a peptide-based hydrogel (**Supplementary Fig. 12, 13**). Upon exposure to gastric fluid, the hydrogel is degraded by pepsin[38] or trypsin[39] (**Supplementary Fig. 14**), which changes the dielectric permittivity of the region above the interdigitated capacitor (ε = 67.4 for peptide hydrogel, ε = 28.1 for gastric fluid), decreases the device's capacitance, and shifts the resonance dip in the harmonic backscattering spectrum (**Supplementary Figure 15**). Ultrasound imaging **(Fig. 4b, Supplementary Video 5)** shows that the suture is located about 2 cm under the skin surface, with slight periodic variations in distance due to respiratory motion. An antenna was placed on the skin surface to wirelessly interrogate the suture in either the frequency- or time- resolved mode through the thick tissues.

Fig. 4c shows the harmonic backscattering spectra wirelessly acquired using the frequency-resolved mode. Two distinct spectra with resonant dip positions corresponding to P1 and P2 can be observed. Artificial gastric fluid (~20 μL, 2500 U/mL pepsin, and pH 2) was injected into the subcutaneous region near P2 to simulate gastric leakage. The position of the resonant dip shifts by 280 MHz (~11% change) within 10 min of injection (**Fig. 4d**), indicating that the WiSe suture can wirelessly detect the presence of gastric fluid. We further tested the ability of the wireless system to detect suture breakage by cutting the suture at a single point immediately adjacent to P2. Due to the change in the suture's electrical length on one side of the pledget, the average power of the harmonic backscattering spectrum measured from the skin surface decreases by 15 dB (**Fig. 4e, Extended Data Fig. 3**), although the average power remains above the noise floor. Separate *ex vivo* experiments show that unraveling of the surgical stitch, such as during wound dehiscence, can also result in >10 dB decrease in the received signal due to reduction of the effective length of the dipole antenna formed by the suture (**Extended Data Fig. 4**). These results suggest that suture integrity can be wirelessly ascertained without visual access to the surgical site.

Time-resolved wireless readout of the WiSe suture provides additional monitoring capabilities that may be useful for physiological monitoring. **Fig. 4f-h** show that the time-resolved signal acquired from the skin surface exhibits periodic variations corresponding to the motion of the muscle layer during respiration (**Fig. 4b**). The respiratory rate (RR) can be clearly extracted as RR=0.2 Hz from the signal spectrogram following low-pass filtering and a continuous wavelet transform (**Fig. 4i, j, Supplementary Fig. 16**). The respiration rate remains clearly distinguishable even after exposing the suture to artificial gastric fluid (**Fig. 4k**). However, breakage of the suture results in loss of the respiratory signal in both the time (**Fig. 4h**) and frequency domains (**Fig. 4l**). While a detectable harmonic signal remains, the periodic pulses are no longer distinguishable because of the decrease in the signal-to-noise ratio and mechanical decoupling of the suture from the motion of the muscle layer after breakage. Time-resolved readout of WiSe sutures applied to a subcutaneous incision in rats allowed detection of respiration with RR=0.28 Hz, indicating the capability of the system to track more rapid physiological motions (**Extended Data Fig. 5**).

WiSe sutures can also be adapted to detect infection of the surgical wound through minor modifications to the electronic pledget. **Supplementary Fig. 17** shows an example in which the electronic pledget is functionalized using a DNA-based hydrogel. When the hydrogel is exposed to deoxyribonuclease, an enzyme commonly secreted by pathogenic microbes[40], hydrogel collapses due to cleavage of the DNA strands, resulting in a wirelessly detectable change in capacitance (**Supplementary Fig. 18**). *In vitro* experiments show that co-incubation of the hydrogel with *S. aureus*, the most common bacteria implicated in wound infections[41], results in complete digestion after 6 hours. In contrast, no substantial change in the size of the hydrogel was observed after 24-hour incubation with human dermal fibroblasts (**Supplementary Fig. 19**). Furthermore, incubation of WiSe sutures functionalized with this hydrogel with amounts of *S. aureus* corresponding to thresholds for clinical infection (10^6 CFU) show a clearly detectable 0.3-GHz shift in the resonant dip of the backscattering spectrum (**Supplementary Fig. 20**). WiSe sutures can also be functionalized to respond to multiple physiological parameters. **Supplementary Fig. 21** shows an illustrative example in which a suture functionalized with both peptide and DNA hydrogels responds to exposure to nuclease (0.3-GHz shift) as well as subsequent exposure to pepsin (0.21-GHz shift). In contrast, WiSe sutures functionalized with either peptide or DNA hydrogels do not exhibit substantial changes in the backscattering spectrum when the pH (**Supplementary Fig. 22**) and ionic strength (**Supplementary Fig. 23**) is varied within physiological ranges.

Chronic wireless sensing and wound healing in rat model

We evaluated the capability of WiSe sutures to provide healing outcomes equivalent to medical-grade sutures while providing chronic wireless sensing using an incisional wound model in rats (**Fig. 5a,b**). Wireless sensing was first evaluated over 14 post-operative days, which is the duration of normal wound healing in rodents and also represents a period within which the vast majority of clinical complications occur[5,6]. Prior to each measurement, a calibration procedure was applied to place the antenna at the position and orientation of maximum signal strength (**Extended Data Fig. 6, Methods**). WiSe sutures applied to deep wounds modelled by an incision on the gluteal muscle responded wirelessly with signal-to-noise ratio greater than 25 dB with no substantial change over the implantation duration. Using an electronic pledget functionalized by peptide hydrogel, the shift in the resonant dip Δf was less than 120 MHz and the change in the receiver power ΔP less than 3.2 dB over 14 days (**Fig. 5d,e**). When the implanted suture is exposed to ~20 μL artificial gastric fluid (2500 U/mL pepsin, pH 2) subcutaneously injected to simulate gastric leakage, the resonant dip increased by Δf = 400 MHz without substantial change in the average received power. Furthermore, severing the suture near the pledget to simulate suture breakage resulted in a large change in received power ΔP = 20 dB and disappearance of the resonant dip. Over the 14-day duration, the respiratory rate can be detected through the time-resolved wireless readout waveform in all cases except after suture breakage (**Extended Data Fig. 7a**).

We next compared healing outcomes between wounds closed by WiSe sutures and unmodified, medical-grade silk sutures. Sutures were applied to either a skin or muscle wound (**Extended Data Fig. 7b,c**), and histological comparisons were performed across four sub-groups on days 1, 4, 7, and 14 post-surgery. Blinded histopathologic scoring of inflammation and healing revealed no substantial difference between the WiSe and control groups across all stages of healing (**Fig. 5f, g**). Histology images show natural wound healing progression in both skin and muscle tissues, including acute inflammation on day 1, granulation tissues with proliferated fibroblasts and neovascularization on day 4, healing with collagen deposition on day 7, and re-organization of granulation tissue with wound closure on day 14. No substantial differences were observed between the control group and experimental group (**Extended Data Fig. 7d,e**). Wound healing processes were further examined using immunofluorescence staining. In both groups, CD3 (inflammatory marker) and fibronectin (healing marker) are absent on day 1, are elevated on day 4, and then persist until

day 14 (**Fig. 5j, k**). These results indicate that the WiSe sutures provide chronic wireless sensing and healing outcomes equivalent to that of the underlying medical-grade silk suture.

Discussion

We have reported materials, designs, and systems that enable medical-grade sutures to be endowed with capabilities for the continuous wireless sensing of physical and chemical parameters at the surgical site. In contrast to previously reported electronic suture technologies, WiSe sutures operate similarly to radiofrequency identification tags, providing wireless and battery-free sensing while maintaining suture-like mechanics. Mechanical and electromagnetic studies establish the operating characteristics of the wireless sensing system and its applicability to a broad range of suture types, surgical stitches, and anatomical regions. With *in vivo* experiments in a porcine model, we have shown multisensor designs capable of detecting breakage of the suture and leakage of gastric fluids deep in the body. Furthermore, chronic studies in rats show robust wireless sensing over two weeks of application on both surface wounds and deep wounds, with healing outcomes that are equivalent to the underlying medical-grade suture.

WiSe sutures may be used to complement or replace existing non-resorbable sutures, clips, and staples to provide continuous monitoring of deep surgical sites. Similar to these surgical devices, WiSe sutures may be removed by a subsequent surgical or endoscopic[42,43] procedure when the risk of complications has passed or may be left indefinitely in the body. Future work will focus on the development of a portable wireless reader to replace the bulky radio-frequency setup currently used to wirelessly read out the WiSe sutures. Our results establish that the power, bandwidth, and sensitivity requirements for wireless operation are well within the specifications of commercially-available radio-frequency integrated circuits[45], such that the system can be implemented as a compact, battery-powered wearable device. This device will enable surveillance of post-operative complications even outside of clinical settings, which has important medical implications for the detection of leakage from gastrointestinal anastomoses[46-48] or monitoring the patency of blood vessels in surgical grafts[49,50]. Further validation of the wireless functionality over time durations relevant to post-operative monitoring, as well as the long-term biocompatibility of the sutures, is needed to establish medical-grade suture performance. Increasing the operating depth will also be important to enable deeper organs and tissues to be monitored. In this regard, advances in the development of more conductive polymers[51] (**Supplementary Note 3**) and wireless techniques to focus radiofrequency signals deeper in the body could be leveraged[52,53]. Future work may also explore the application of the developed wireless techniques and systems to other advanced suture-based sensing approaches[21,54] as well as emerging concepts in resorbable bioelectronics[15,18,55,56].

Methods

Suture functionalization process

WiSe sutures were prepared by functionalizing medical-grade silk sutures (size 0, Ethicon, Johnson & Johnson). Silk sutures were first treated with oxygen plasma for 2 minutes to remove the waxy coating and then soaked in *N*-Methyl-2-pyrrolidone (NMP, Sigma Aldrich) for 20 minutes to further clear wax and render hydrophilicity. Next, the sutures were soaked in a solution of poly(3,4-ethylenedioxythiophene)-poly(styrene sulfonate) (PEDOT:PSS, Clevios PH1000, Heraeus) with 5% Dimethyl Sulfoxide (DMSO, Sigma Aldrich) for 30 minutes, and dried in vacuum oven for 1 hour to ensure the absorption of PEDOT:PSS by silk filaments. Soaking and drying were repeated for 3 cycles to achieve a uniform conductive coating with the desired conductance. Finally, the sutures were coated by parylene-C (~1 μm thickness, **Supplementary Fig. 3**) using chemical vapor deposition (LAVIDA, FEMTO Science) to form a biocompatible encapsulation layer. To create an insulating region for the electronic pledget, a segment of the silk suture (2 mm length) was coated with silicone before functionalization. Fabricated sutures were sterilized using autoclave (121 °C, 20 min, Hirayama HV-110) prior to use.

Mechanical, electrical, and biocompatibility tests

Tensile strength measurements were performed using a universal testing machine (LR 10K) and tissue drag measurements with a linear stage (NLE-Linear) with force gauge (M5i-Force, Mark-10). Biocompatibility tests were performed by incubating human dermal fibroblasts (HDFs) and keratinocytes (HaCaT) with medical-grade silk sutures (size 0, Ethicon-Johnson and Johnson), PEDOT:PSS-coated silk sutures, and parylene-C encapsulated WiSe sutures in a Transwell chamber (6.5-mm membrane diameter, 0.4-μm pore size, Corning). Cell viability was assessed using the MTS assay after co-incubation with the suture for 72 hours.

The electrical properties of the WiSe sutures were characterized through infrared imaging and resistance measurements. A thermal camera (E5, FLIR Systems) was used to image the thermal distribution of the suture during Joule heating (30 V DC voltage) starting at room temperature. Knotting tests were performed by wrapping the sutures around 3D-printed cylindrical rods with radii ranging from 50 mm to 1 mm. The resistances of the sutures with knot were measured using a digital multimeter (Keysight 34461A). Soak tests were performed using PEDOT:PSS-coated sutures (1 cm length) and WiSe sutures (1 cm length with parylene-C encapsulation) in 1× phosphate buffered saline solution.

Electronic pledget design

The electronic pledget was assembled on a flexible printed-circuit board fabricated by printing the circuit traces shown in **Supplementary Fig. 1** on a copper-polyimide substrate (18-μm-thick copper, 25-μm-thick polyimide layer, DuPont). After elevating to 70 °C for 10 min in order to enhance the uniformity of the ink on the copper, the circuit board was etched using H_2O_2 and HCl and cleaned by immersion in hexane and ethanol to yield the patterned traces. A surface-mount Schottky diode (Skyworks Solution, SMS7630-079LF) and 12-nH inductor (Würth Elektronik, 744765112A) was soldered onto the circuit board using lead-free solder paste (Chip Quik, SMDLTLFP). The circuit board was then encapsulated by surgical silicone adhesive (~0.1 mm thickness, Kwik-Sil Adhesive), exposing the holes for threading the suture. To functionalize the capacitive sensor, two silicone pillars (~1 mm thickness) was added onto the capacitive sensor surface for mechanical support. Pledgets were sterilized by immersion into Cidex OPA solution at room temperature for 10 min before functionalization.

Harmonic measurement system

The wireless system in **Supplementary Fig. 8a** was built from the following components: (1) signal generator (SMB 100A, Rohde & Schwarz), (2) power amplifier (43 dB gain, ZHL-10W-2G+, Mini-Circuits), (3) low-pass filters (PASTERNACK, PE87FL1013; CRYSTEK, CLPFL-1600), (4) directional coupler (10 dB, PASTERNACK PE2209-10), (5) high-pass filters (PASTERNACK, PE87FL1019, PE87FL1013), (6) spectrum analyzer (N9000B, Keysight), (7) customized wideband dipole antenna, and (8) coaxial cables (SMA-SMA, 50 Ω, Amphenol). LabVIEW (National Instruments) was used to control and synchronize the signal generation and data collection process.

Transmission and reception of the wireless signals used a custom-designed wideband antenna (**Supplementary Fig. 7**). Frequency-resolved readout was performed by sweeping the frequency of the transmit signal from 1 to 2 GHz at the same transmit power, while recording the power of the received harmonic signal using the spectrum analyzer. The measured harmonic backscattering spectrum exhibits a dip resulting from the effective short-circuiting of the Schottky diode at the resonant frequency of the series *LC* tank. The signal-to-noise ratio (SNR) is defined as the average signal power above the noise floor (-120 dBm) over the operating frequency range. Time-resolved readout was performed by transmitting a signal and measuring the power of the received harmonic signal with a sampling frequency of 25 Hz.

Reader antenna positioning

The reader antenna was positioned for suture readout using a two-step procedure to provide maximum reception of the backscattered signal and comparable power levels between measurements (**Extended Data Fig. 6a**). First, the position of the antenna was scanned within a 40 mm × 40 mm area over the target region. The antenna position is set to be within the 10 mm × 10 mm area providing the highest signal amplitude (**Extended Data Fig. 6b,c**). Second, the antenna is rotated from 0° to 90° to establish the optimal orientation relative to the suture. The angle of the antenna is set to be within 15° of the highest signal amplitude (**Extended Data Fig. 6d,e**). The baseline power level is obtained by averaging the power of the harmonic backscattering spectrum across the operating frequency. For suture breakage detection, breakage is deemed to have occurred when the average power level recorded at a subsequent time point after performing the calibration steps decreases by more than 10 dB.

Peptide hydrogel synthesis

To synthesize the peptide hydrogel, 10 wt% gelatin powder (Sigma Aldrich) was dissolved in deionized water at ~90 °C to form the precursor solution. After allowing the precursor to cool to ~40 °C, a cross-linking agent (0.35 wt% glutaraldehyde) was added into the precursor and the solution thoroughly mixed. After allowing ~10 min for the cross-linking reaction, the solution formed a viscous gel that was transferred to the surface of

the interdigitated capacitor, resulting in a pepsin-responsive sensor. To test the sensor, artificial gastric fluid was prepared using pepsin from porcine gastric mucosa (Sigma Aldrich). 2500 U/mL pepsin stock solution (pH 2) was prepared by adding hydrochloric acid (Sigma Aldrich). For the *in vitro* test, the peptide hydrogel was exposed to ~10 μL pepsin solution at 37 °C for 10 min.

In vivo deep wound sensing experiments

In vivo sensing experiments used a female Landrace cross pig (6 months old, 52 kg) acquired from the Singapore National Large Animal Research Facility to demonstrate multi-nodal sensing with the WiSe suture. Pig was premedicated with intramuscular ketamine (10mg/kg), atropine (0.04mg/kg) and midazolam (0.6mg/kg), induced with 4% isoflurane, intubated and maintained with 1-2% isoflurane throughout the experiments. To model the surgical wound, a 10-cm incision was made over the left latissimus dorsi region using a surgical scalpel to expose the muscle layer. A 10-cm sharp incision was subsequently made on the exposed muscle and the WiSe suture was used to close the muscle wound using a continuous stitch. During suturing, two pledgets functionalized using the peptide hydrogel were attached to the suture approximately 5 cm apart, oriented such that the sensor faces the muscle tissues. The wound was then closed using wound dressing (Tegaderm, 3M) to secure the skin incision. To model gastric leakage, artificial gastric fluid (~20 μL, 2500 U/mL pepsin, pH 2) was injected using a syringe within 5 mm of a pledget. Wireless measurement of the harmonic backscattering spectrum was then performed by placing an antenna on the skin surface approximately 2 cm above the wound site (see Harmonic measurement system). Next, suture breakage was modeled by opening the wound and severing the suture near a pledget. After closing the wound again with wound dressing, wireless measurements were performed using the same process. The animal was euthanized after the experiment. All experiments conformed to the Guide for the Care and Use of Laboratory Animals published by the National Institutes of Health, USA, and protocol approved by the Institutional Animal Care and Use Committee (IACUC), National University of Singapore.

In vivo wound healing experiments

Male Sprague-Dawley rats (age 5-6 months, 350-500 g) were used to demonstrate wound healing and wireless sensing over 14 days[57,58]. Surgery was performed under isoflurane (1-3%) inhalation anaesthesia. A surgical wound was created by either making a 2-cm skin incision on the skin of the lower back region (skin group) or exposing the gluteal muscle by blunt dissection and making a 2-cm incision (muscle group) using a scalpel. A WiSe suture with a single attached single pledget (functionalized using the hydrogel) was used to close the wound using a continuous stitch and surgeon's square knots, with pledget oriented such that the sensor faces the wound. For the muscle group, the skin was closed over the wound using an unmodified medical-grade suture. Gastric leakage in **Extended Data Fig. 5** was modeled by subcutaneously injecting ~20 μL artificial gastric fluid with pepsin (2500 U/mL, pH 2) near the pledget. Suture breakage in **Extended Data Fig. 5** was simulated by severing the suture near the center of the stitch, adjacent to the electronic pledget. Following surgery, antibiotic Enrofloxacin (10 mg/kg) was subcutaneously administered daily for 5 days and Buprenorphine (0.05 mg/kg) analgesia twice a day for 3 days. All experiments conformed to the Guide for the Care and Use of Laboratory Animals published by the National Institutes of Health, USA, and protocol approved by the Institutional Animal Care and Use Committee (IACUC), National University of Singapore.

Histoprocessing and evaluation

Tissues obtained from wound excision areas at skin and muscle tissues were fixed in 10% neutral buffered formalin. The tissues were then processed, embedded and cut at 5 μm thickness and stained with Hematoxylin & Eosin staining. Histological assessments were performed in a blinded fashion by the histopathologist for the presence of inflammation, necrosis, crust, granulation tissue, collagen deposition, re-epithelization, and neovascularization following the scoring pattern of 0 to 3, (0 indicates none; 1, scant; 2, moderate; and 3, abundant) as described previously[59].

Immunofluorescence staining

To demonstrate fibronectin, after deparaffinisation, antigen-retrieval was performed in epitope retrieval solution (BOND, pH6, Leica). After blocking with 10% goat serum, the tissues were incubated overnight with rabbit anti rat fibronectin (Cat# SAB4500974, Sigma Aldrich) at the dilution of 1:50 at 4° C. Then, the slides were treated with goat anti-rabbit antibody with Alexa 594 (Cat # A11012, Life technologies) at 1:500 for 30 minutes followed by a mounting medium using a DAPI mountant (Vectashield HardSet, Vector Laboratories).

CD3 staining followed the same protocol except with the following modifications: epitope retrieval solution (BOND, pH9, Leica), polyclonal rabbit anti-human CD3 (Cat# A0452, Dako) at the dilution of 1:50 and goat anti-rabbit with Alexa 488 (Cat # A11034, Life technologies) at 1:500. The images were acquired through NIS Elements Imaging software (Version-5.02, Nikon) using DS Fi3 camera (Nikon) fitted on Eclipse 90i fluorescence microscope (Nikon).

In vitro detection of pathogenic bacteria

Bacterial infection detection experiments used a sensor functionalized by DNA hydrogel[60]. DNA precursor was prepared by dissolving 10 wt% deoxyribonucleic acid sodium salt (smDNA) in 4.0 mM NaBr solution. 2.5 wt% crosslinker, 1,4-Butanediol diglycidyl ether (BDDE), was uniformly mixed with the precursor and 0.5 wt% *N*,*N*,*N'*,*N'*-Tetramethylethylenediamine (TMEDA) as the catalyst was mixed with the hydrogel precursor. The hydrogel precursor was then loaded on the interdigital capacitor of the electronic pledget and was further transferred into a 1.5 mL centrifuge tube and immersed into a water bath at 85 °C for 2 h to complete the gelation. After the gelation, the prepared DNA hydrogel was rinsed by DI water to remove unreacted chemicals.

Staphylococcus aureus (*S. aureus*) was sub-cultured in Brain Heart Infusion broth (BHI, Sigma Aldrich) and incubated at 37˚C overnight. Cell culture media, containing secreted extracellular nuclease, was extracted and dropped on the DNA hydrogel. Confocal images in **Supplementary Fig. 19 and 20** were acquired using a confocal microscope (Olympus FV1000) using a bacterial viability stain (LIVE/DEAD BacLight Bacterial Viability Kit, Invitrogen, Thermo Fisher Scientific) for the *S. aureus* and a fluorescence stain (NucBlue, Invitrogen, Thermo Fisher Scientific) for the DNA hydrogel. For the control experiment, human dermal fibroblasts (HDFs) were sub-cultured in Dulbecco's Modified Eagle Medium (DMEM, Sigma Aldrich) and co-incubated with DNA hydrogel over a period of 6-24 hours to allow cell adhesion on the surface of the hydrogel. Fluorescent images of the cells were acquired using a plasma membrane stain (CellMask, Invitrogen, Thermo Fisher Scientific).

Electromagnetic simulations

Electromagnetic simulations used the finite-difference time-domain method (CST Microwave Studio, Dassault Systems) to evaluate the wireless system performance and design the interdigitated capacitor. All simulations are performed with suture placed in muscle tissue (dielectric permittivity of $\varepsilon_r = 54.8 + i12.77$ at 2.4 GHz) unless otherwise indicated (e.g. human body model). SAR studies used an anatomically accurate human body model (Gustav, CST Voxel family) with all organs and tissue structures (resolution of 2.08 × 2.08 × 2 mm) using a 10-g averaging mass as described in the IEEE/IEC 62704-1 standard.

Reporting Summary. Further information on research design is available in the Nature Research Reporting Summary linked to this article.

Data availability

The main data supporting the findings of this study are available within the paper and its Supplementary Information. Source data for Fig. 5f,g are provided with this paper. Other raw and analysed datasets generated during the study are available for research purposes from the corresponding authors on reasonable request.

References

1. Anderson, O., Davis, R., Hanna, G. B. & Vincent, C. A. Surgical adverse events: a systematic review. *Am. J. Surg.* **206**, 253-262 (2013).

2. Maday, K. R., Hurt, J. B., Harrelson, P. & Porterfield, J. Evaluating postoperative fever. *J. Am. Acad. PAs.* **29**, 23-28 (2016).

3. Blouw, E. L., Rudolph, A. D., Narr, B. J. & Sarr, M. G. The frequency of respiratory failure in patients with morbid obesity undergoing gastric bypass. *AANA J.* **71**, 45-50 (2003).

4. Endara, S. A., Serrano, A. J., Sandoval, B. A. & Davalos, G. A. Esophageal perforation during gastric bypass: delayed diagnosis and management. *Obes. Surg.* **17**, 986-988 (2007).

5. Kazaure, H. S., Roman, S. A. & Sosa, J. A. Association of postdischarge complications with reoperation and mortality in general surgery. *Arch. Surg.* **147**, 1000-1007 (2012).

6. Woodfield, J. C., Jamil, W. & Sagar, P. M. Incidence and significance of postoperative complications occurring between discharge and 30 days: a prospective cohort study. *J. Surg. Res.* **206**, 77-82 (2016).

7. Pour-Ghaz, I., Hana, D., Raja, J., Ibebuogu, U. N. & Khouzam, R. N. CardioMEMS: where we are and where can we go? *Ann. Transl. Med.* **7**, 1-7 (2019).

8. Steiger, C. *et al*. Ingestible electronics for diagnostics and therapy. *Nat. Rev. Mater.* **4**, 83-98 (2019).

9. Kong, Y. L. *et al*. 3D-printed gastric resident electronics. *Adv. Mater. Technol.* **4**, 1800490 (2019).

10. Someya, T., Bao, Z. & Malliaras, G. G. The rise of plastic bioelectronics. *Nature* **540**, 379-385 (2016).

11. Yang, Y. & Gao, W. Wearable and flexible electronics for continuous molecular monitoring. *Chem. Soc. Rev.* **48**, 1465-1491 (2019).

12. Choi, S. *et al*. Highly conductive, stretchable and biocompatible Ag–Au core–sheath nanowire composite for wearable and implantable bioelectronics. *Nat. Nanotechnol.* **13**, 1048-1056 (2018).

13. Chung, H. U. *et al*. Binodal, wireless epidermal electronic systems with in-sensor analytics for neonatal intensive care. *Science* **363**, eaau0780 (2019).

14. Boutry, C. M. *et al*. A stretchable and biodegradable strain and pressure sensor for orthopaedic application. *Nat. Electron.* **1**, 314-321 (2018).

15. Tao, H. *et al*. Silk-based resorbable electronic devices for remotely controlled therapy and in vivo infection abatement. *Proc. Natl. Acad. Sci.* **111**, 17385-17389 (2014).

16. Wang, C. *et al*. Monitoring of the central blood pressure waveform via a conformal ultrasonic device. *Nat. Biomed. Eng.* **2**, 687-695 (2018).

17. Boutry, C. M. *et al*. Biodegradable and flexible arterial-pulse sensor for the wireless monitoring of blood flow. *Nat. Biomed. Eng.* **3**, 47-57 (2019).

18. Burton, A. *et al*. Wireless, battery-free subdermally implantable photometry systems for chronic recording of neural dynamics. *Proc. Natl. Acad. Sci.* **117**, 2835-2845 (2020).

19. Kim, D.-H. *et al*. Thin, flexible sensors and actuators as 'instrumented' surgical sutures for targeted wound monitoring and therapy. *Small* **8**, 3263-3268 (2012).

20. Mostafalu, P. *et al*. A toolkit of thread-based microfluidics, sensors, and electronics for 3D tissue embedding for medical diagnostics. *Microsyst. Nanoeng.* **2**, 16039 (2016).

21. Wang, L. *et al*. Functionalized helical fibre bundles of carbon nanotubes as electrochemical sensors for long-term in vivo monitoring of multiple disease biomarkers. *Nat. Biomed. Eng.* **4**, 159-171 (2020).

22. Owyeung, R. E., Terse-Thakoor, T., Rezaei Nejad, H., Panzer, M. J. & Sonkusale, S. R. Highly flexible transistor threads for all-thread based integrated circuits and multiplexed diagnostics. *ACS Appl. Mater. Inter.* **11**, 31096-31104 (2019).

23. Terse-Thakoor, T. *et al*. Thread-based multiplexed sensor patch for real-time sweat monitoring. *npj Flex. Electron.* **4**, 18 (2020).

24. Liu, M. *et al*. Biomimicking antibacterial opto-electro sensing sutures made of regenerated silk proteins. *Adv. Mater.* **33**, 2004733 (2021).

527 25. Stuart, T., Cai, L., Burton, A. & Gutruf, P. Wireless, battery-free platforms for collection of biosignals.
528 *Biosens. Bioelectron.*, 113007 (2021).

529 26. Mondal, S. & Chahal, P. A passive harmonic RFID tag and interrogator development. *IEEE J. Radio*
530 *Freq. Identif.* **3**, 98-107 (2019).

531 27. Vera, G. A., Duroc, Y. & Tedjini, S. Third harmonic exploitation in passive UHF RFID. *IEEE Trans.*
532 *Microw. Theory Tech.* **63**, 2991-3004 (2015).

533 28. Li, P., An, Z., Yang, L., Yang, P. & Lin, Q. RFID harmonic for vibration sensing. *IEEE Trans. Mob.*
534 *Comput.* **20**, 1614 - 1626 (2019).

535 29. Wang, Y. *et al*. A highly stretchable, transparent, and conductive polymer. *Sci. Adv.* **3**, e1602076 (2017).

536 30. Rivnay, J. *et al*. Organic electrochemical transistors. *Nat. Rev. Mater.* **3**, 17086 (2018).

537 31. Maehara, Y. *et al*. Impact of intra-abdominal absorbable sutures on surgical site infection in
538 gastrointestinal and hepato-biliary-pancreatic surgery: results of a multicenter, randomized, prospective,
539 phase II clinical trial. *Surg. Today* **47**, 1060-1071 (2017).

540 32. Pirtea, L., Balint, O., Secosan, C., Grigoras, D. & Ilina, R. Laparoscopic pectopexy with burch
541 colposuspension for pelvic prolapse associated with stress urinary incontinence. *J. Minim. Invasive Gynecol.*
542 **27**, 1023-1024 (2020).

543 33. IEEE standard for safety levels with respect to human exposure to radio frequency electromagnetic
544 fields, 3 kHz to 300 GHz. *IEEE Std C95.1-2005 (Revision of IEEE Std C95.1-1991)*, 1-238 (2006).

545 34. Gabriel, S., Lau, R. W. & Gabriel, C. The dielectric properties of biological tissues: III. parametric models
546 for the dielectric spectrum of tissues. *Phy. Med. Biol.* **41**, 2271-2293 (1996).

547 35. Keat Ghee, O., Kefeng, Z. & Grimes, C. A. A wireless, passive carbon nanotube-based gas sensor. *IEEE*
548 *Sens. J.* **2**, 82-88 (2002).

549 36. Feng, Y., Xie, L., Chen, Q. & Zheng, L. Low-cost printed chipless RFID humidity sensor tag for intelligent
550 packaging. *IEEE Sens. J.* **15**, 3201-3208 (2015).

551 37. Mannoor, M. S., Zhang, S., Link, A. J. & McAlpine, M. C. Electrical detection of pathogenic bacteria via
552 immobilized antimicrobial peptides. *Proc. Natl. Acad. Sci.* **107**, 19207-19212 (2010).

553 38. Foltz, E. *et al*. An assessment of human gastric fluid composition as a function of PPI usage. *Physiol.*
554 *Rep.* **3**, e12269 (2015).

555 39. Engelking, L. R. *Textbook of Veterinary Physiological Chemistry (third edition)* 39-44 (Academic Press,
556 2015).

557 40. Sharma, P., Garg, N., Sharma, A., Capalash, N. & Singh, R. Nucleases of bacterial pathogens as
558 virulence factors, therapeutic targets and diagnostic markers. *Int. J. Med. Microbiol.* **309**, 151354 (2019).

559 41. Giacometti, A. *et al*. Epidemiology and microbiology of surgical wound infections. *J. Clin. Microbiol.* **38**,
560 918-922 (2000).

561 42. Backes, F. J., Cohn, D. E., Mannel, R. S. & Fowler, J. M. in *Clinical Gynecologic Oncology (ninth edition)*
562 560-578.e511 (Elsevier, 2018).

563 43. Bège, T. *et al*. An endoscopic strategy for management of anastomotic complications from bariatric
564 surgery: A prospective study. *Gastrointest. Endosc.* **73**, 238-244 (2011).

565 44. Hwang, S.-W. *et al*. A physically transient form of silicon electronics. *Science* **337**, 1640-1644 (2012).

45. Karmakar, N. C., Koswatta, R., Kalansuriya, P., & Rubayet, E. *Chipless RFID Reader Architecture*. (Artech House, 2013).

46. Li, Y. *et al*. Very early colorectal anastomotic leakage within 5 post-operative days: a more severe subtype needs relaparatomy. *Sci. Rep.* **7**, 39936 (2017).

47. Slieker, J. C., Daams, F., Mulder, I. M., Jeekel, J. & Lange, J. F. Systematic review of the technique of colorectal anastomosis. *JAMA Surg.* **148**, 190-201 (2013).

48. Gonzalez, R. *et al*. Diagnosis and contemporary management of anastomotic leaks after gastric bypass for obesity. *J. Am. Coll. Surgeons* **204**, 47-55 (2007).

49. Han, S., Proctor, A. R., Ren, J., Benoit, D. S. W. & Choe, R. Temporal blood flow changes measured by diffuse correlation tomography predict murine femoral graft healing. *PLoS One* **13**, e0197031 (2018).

50. Barbu, A., Jansson, L., Sandberg, M., Quach, M. & Palm, F. The use of hydrogen gas clearance for blood flow measurements in single endogenous and transplanted pancreatic islets. *Microvasc. Res.* **97**, 124-129 (2015).

51. Wu, F. *et al*. Conductivity enhancement of PEDOT:PSS via addition of chloroplatinic acid and its mechanism. *Adv. Electron. Mater.* **3**, 1700047 (2017).

52. Ho, J. S. *et al*. Wireless power transfer to deep-tissue microimplants. *Proc. Natl. Acad. Sci.* **111**, 7974-7979 (2014).

53. Agrawal, D. R. *et al*. Conformal phased surfaces for wireless powering of bioelectronic microdevices. *Nat. Biomed. Eng.* **1**, 0043 (2017).

54. Lee, J. *et al*. Stretchable and suturable fibre sensors for wireless monitoring of connective tissue strain. *Nat. Electron.* **4**, 291-301 (2021).

55. Cha, G. D., Kang, D., Lee, J. & Kim, D.-H. Bioresorbable electronic implants: history, materials, fabrication, devices, and clinical applications. *Adv. Healthc. Mater.* **8**, 1801660 (2019).

56. Kang, S.-K., *et al*. Bioresorbable silicon electronic sensors for the brain. *Nature* **530**, 71-76 (2016).

57. Dorsett-Martin, W. A. Rat models of skin wound healing: a review. *Wound Repair Regen.* **12**, 591-599 (2004).

58. Obuobi, S. *et al*. Phenylboronic acid functionalized polycarbonate hydrogels for controlled release of polymyxin B in pseudomonas aeruginosa infected burn wounds. *Adv. Healthc. Mater.* **7**, 1701388 (2018).

59. Abramov, Y. *et al*. Histologic characterization of vaginal vs. abdominal surgical wound healing in a rabbit model. *Wound Repair Regen.* **15**, 80-86 (2007).

60. Topuz, F. & Okay, O. Rheological behavior of responsive DNA hydrogels. *Macromolecules* **41**, 8847-8854 (2008).

61. Raymer, D. M. & Smith, D. E. Spontaneous knotting of an agitated string. *Proc. Natl. Acad. Sci.* **104**, 16432-16437 (2007).

Acknowledgements

The authors thank Z. Goh for assisting in the art in Fig. 1a; A. Bansal and H. Li for supporting the *in vitro* experiments; and Y.X. Guo for facilitating the dielectric measurements. J.S.H. acknowledges support from grants from the National Research Foundation Singapore (NRFF2017-07 and AISG-GC-2019-002), Ministry of Education Singapore (MOE2016-T3-1-004), and Institute for Health Innovation and Technology. P.L.R.E. acknowledges funding provided by the Ministry of Education Singapore (R148000240114). Part of the work was performed in the National University of Singapore Medicine Confocal Microscopy Unit.

Author contributions

V.K., X.Y., Z.X., and J.S.H. designed and performed the research. R.R.L., J.W.W., and C.J.C. performed the large animal studies. H.Y., H.G., and B.C.K.T. performed the mechanical testing experiments. R.R. conducted the histopathological studies. S.O., P.S., D.M., P.L.R.E., and W.L. performed to the *in vitro* experiments and contributed materials. X.G. and J.O. assisted in the design to the fabrication process and contributed materials. X.T., S.K.A., and Z.L. supported the design and characterization of the wireless system. C.S.C. contributed to the study design. V.K., Z.X., and J.S.H. wrote the paper with input from all the authors.

Competing interests

The authors declare no competing interests.

Additional information

Supplementary information The online version contains supplementary material available at https://doi.org/10.1038/s41551-01X-XXXX-X.

Correspondence and requests for materials should be addressed to V.K., Z.X. or J.S.H.

Peer review information *Nature Biomedical Engineering* thanks Keat Ghee Ong, Sameer Sonkusale and the other, anonymous, reviewer(s) for their contribution to the peer review of this work.

Reprints and permissions information is available at www.nature.com/reprints.

Publisher's note: Springer Nature remains neutral with regard to jurisdictional claims in published maps and institutional affiliations.

Fig. 1 | Wirelessly responsive sutures for monitoring deep surgical wounds. a, Illustration of the wireless sensing concept. WiSe sutures are functionalized with a conductive polymer (PEDOT:PSS) and transmit sensing data by modulating the harmonic backscatter signal, which can be measured by the external wireless system. **b**, Surgical use of the WiSe suture. During the procedure of the surgical stitch, an electronic pledget is attached and encapsulated in medical silicone. **c**, Schematic and equivalent electrical circuit of the electronic pledget. The pledget incorporates a nonlinear element (Schottky diode), a capacitive sensor (*C*), and a tuning inductor (*L*), while the suture functions as a dipole antenna. **d**, Wireless readout of the sutures in the frequency-resolved mode. The capacitive sensor transduces changes in the physiological environment, such as due to infection or leakage, into shifts in the resonant dip of the harmonic signal spectrum measured by the wireless system. **e**, Wireless readout of the sutures in the time-resolved mode. Changes in the electrical length of the suture, such as due to breakage and tissue motions, result in temporal variations in the backscattered harmonic signal.

Fig. 2 | Suture functionalization and characterization. a, Schematic of the functionalization process for a multifilament medical-grade silk suture. False color scanning electron microscope images show the surfaces of the suture before functionalization, after coating with PEDOT:PSS, and final encapsulation with parylene-C. **b**, Infrared image of a WiSe suture subject to Joule heating (30 V end-to-end). **c**, Stress-strain response (tensile test) of the WiSe suture and medical-grade sutures. Red curves indicate multifilament sutures (cotton, silk, and polyester) and blue curves represent monofilament sutures (polyglycolic acid (PGA) and nylon). **d**, Tissue drag force per unit circumference required to pull the sutures through synthetic skin. **e**. Viability of human dermal fibroblasts after 72 h co-incubation with the unmodified silk suture, non-insulated suture (coated with PEDOT:PSS but without parylene-C), and WiSe suture. Error bars show the mean ± s.d. (n = 5 samples). **f**, Electrical resistance of a WiSe suture (10 cm length) over 2500 cycles of bending. **g**, Changes in electrical resistance of the WiSe suture as a function of the radius-of-curvature r. Error bars show the mean ± s.d. (n = 3 samples). **h**, Changes in electrical resistance when non-insulated sutures and WiSe sutures are submerged in PBS solution. Error bars show the mean ± s.d. (n = 3 samples).

Fig. 3 | Wireless system design and performance. a, Schematic of the wireless system. L, length of the surgical stitch; d, depth of the suture from the skin. **b**, Electric field distribution of the transmitted (f_0) and backscattered ($2f_0$) signals in a computational human body model including internal organs. WiSe suture is placed on the stomach wall 5 cm below the skin. Solid white line shows the outline of human body and the stomach in the sagittal cross-section. **c-e**, Images and radio-frequency current distributions of WiSe sutures using the Lembert (0.65 kΩ cm^{-1}) (**c**), lock-stitch (1.2 kΩ cm^{-1}) (**d**), and Cushing stitches (0.55 kΩ cm^{-1}) (**e**). **f-h**, Operating region of the wireless system in parameters L and d. P, power of the received harmonic signal at a transmit power of 30 dBm for the Lembert (**f**), lock-stitch (**g**), and Cushing stitches (**h**), where white, black and red lines are the contour lines for the power levels -100 dBm, -110 dBm and -120 dBm respectively. **i-k**, Measured harmonic backscattering spectrum for different values of the sensor capacitance C at length L = 20 mm and varying depths.

Fig.4 | *In vivo* post-operative monitoring. a, Illustration of the experimental setup for wound monitoring in a porcine model. A WiSe suture with two attached electronic pledgets (P1 and P2) is used to close a deep incision on the muscle. **b**, Ultrasound imaging of the suture shows that the pledget is located about 2 cm from the skin surface. Tracking a single pixel line with time shows motion of the muscle layer during respiration. **c-e**, Frequency-resolved wireless readout of the WiSe suture upon application of the suture (**c**), gastric leakage (**d**), and suture breakage (**e**). Gastric leakage is simulated by subcutaneous injection of artificial gastric fluid and breakage by severing the suture near the position of P2. **f-h**, Time-resolved wireless readout of the WiSe suture upon application of the suture (**f**), gastric leakage (**g**), and suture breakage (**h**). **i-l**, Spectrogram (continuous wavelet transform) of the time-resolved signal. White arrows show spectral peaks corresponding to the respiratory rate (RR).

Fig. 5 | Chronic wireless sensing and wound healing outcomes. a, Illustration of WiSe sutures applied to an incision on either the skin or muscle of a rat. **b,** Image of a WiSe suture used to close a muscle incision. **c**, Signal-to-noise ratio (SNR) of the wireless readout from WiSe sutures applied on muscle over 14 days. Box plots show mean, upper quartile, and lower quartile (n = 5 rats). **d,** Change in resonant frequency Δf and received power ΔP of a peptide hydrogel-functionalized WiSe suture applied on muscle over 14 days (n = 1 rat). The suture is subjected to simulated gastric leakage and subsequent breakage on day 14. Dashed lines and cross indicate that no resonant dip is detected. **e,** Normalized harmonic backscattering spectra corresponding to (**d**) Dashed lines and shaded area show mean ± s.d. (n = 4 wireless measurements on day 1, 4, 7 and 14) before the suture is subjected to the simulated event. **f**, **g**, Histopathologic scores for inflammation and healing from skin (**f**) and muscle (**g**) tissues around the suture on days 1, 4, 7, and 14 post-operation. Error bars show the mean ± s.d. (control group: n = 3 rats, test group: n = 5 rats). **j**, **k**, Representative immunofluorescence-stained tissue sections obtained near the sutures. Blue, DAPI stain;

686 green, CD3 stain; red, fibronectin stain. Yellow arrows show T-cell infiltration in the wound tissues. Scale
687 bars, 50 μm.

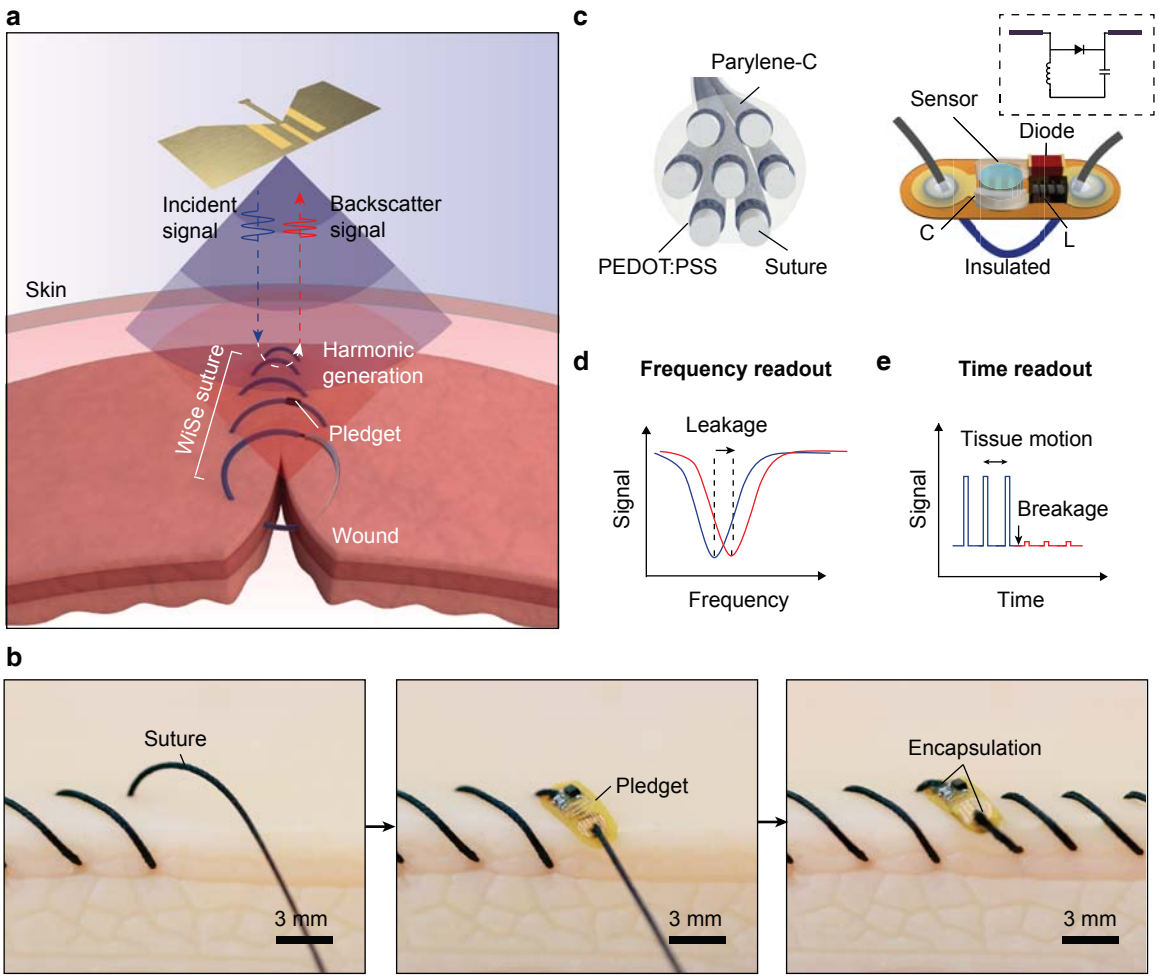
a
Incident signal
Backscatter signal
Skin
Harmonic generation
WiSe suture
Pledget
Wound
c
Parylene-C
PEDOT:PSS
Suture
Sensor
Diode
C
L
Insulated
d
Frequency readout
Leakage
Signal
Frequency
e
Time readout
Tissue motion
Breakage
Signal
Time
b
Suture
3 mm
Pledget
3 mm
Encapsulation
3 mm

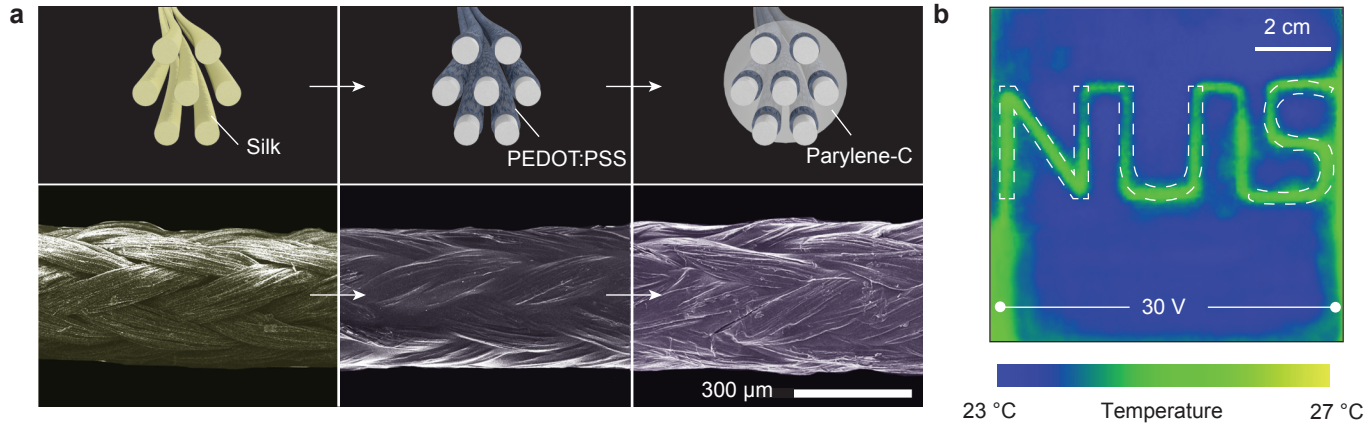
a
Silk
PEDOT:PSS
Parylene-C
300 μm
b
2 cm
30 V
23 °C
Temperature
27 °C

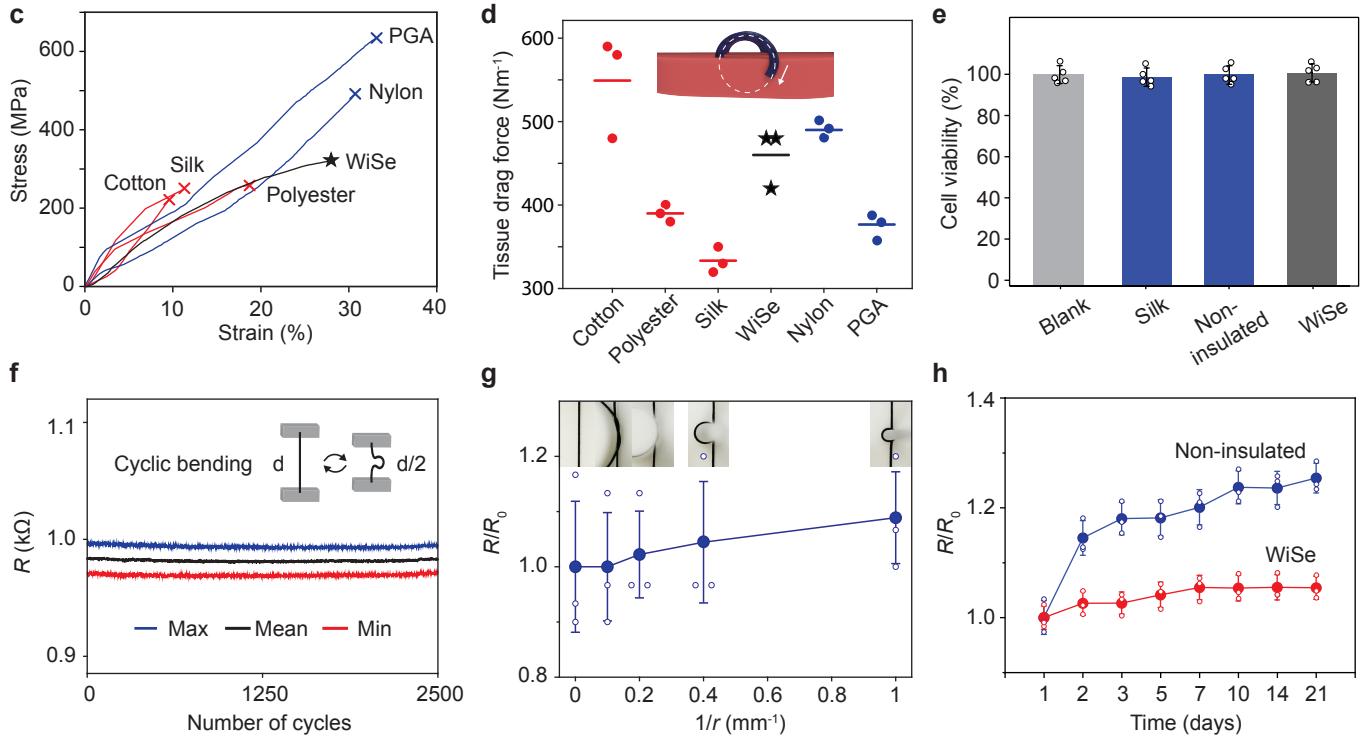
c
Stress (MPa)
Strain (%)
PGA
Nylon
WiSe
Silk
Cotton
Polyester
d
Tissue drag force (Nm⁻¹)
Cotton
Polyester
Silk
WiSe
Nylon
PGA
e
Cell viability (%)
Blank
Silk
Non-insulated
WiSe

f
R (kΩ)
Cyclic bending
d
d/2
Max
Mean
Min
Number of cycles
g
R/R0
1/r (mm⁻¹)
h
R/R0
Non-insulated
WiSe
Time (days)

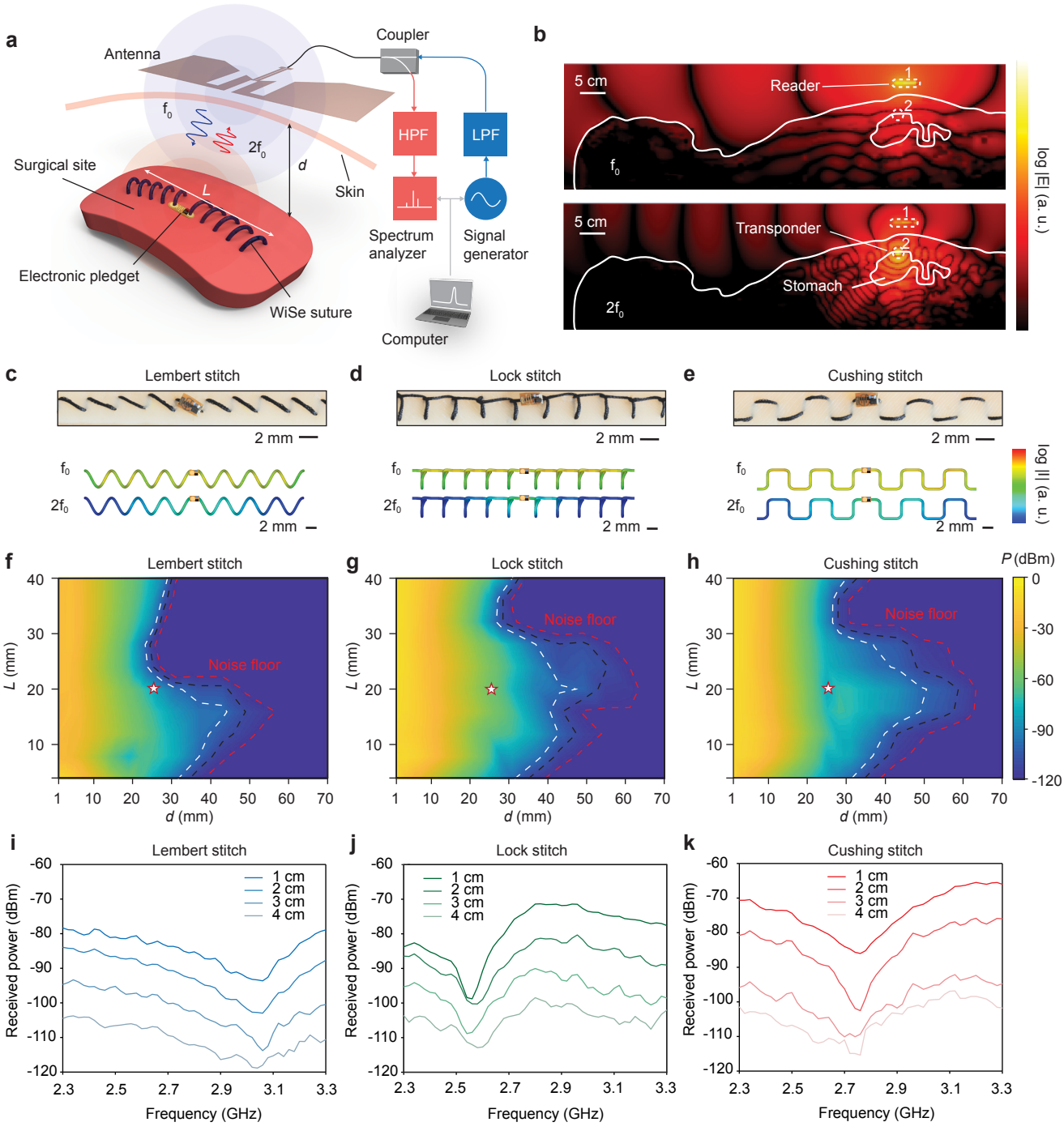
a
Antenna
Coupler
HPF
LPF
Surgical site
Skin
Spectrum analyzer
Signal generator
Electronic pledget
WiSe suture
Computer
b
5 cm
Reader
Transponder
Stomach
log |E| (a. u.)
c
Lembert stitch
d
Lock stitch
e
Cushing stitch
2 mm
log ||
f
Lembert stitch
g
Lock stitch
h
Cushing stitch
Noise floor
L (mm)
d (mm)
P (dBm)
i
Lembert stitch
j
Lock stitch
k
Cushing stitch
Received power (dBm)
Frequency (GHz)
1 cm
2 cm
3 cm
4 cm

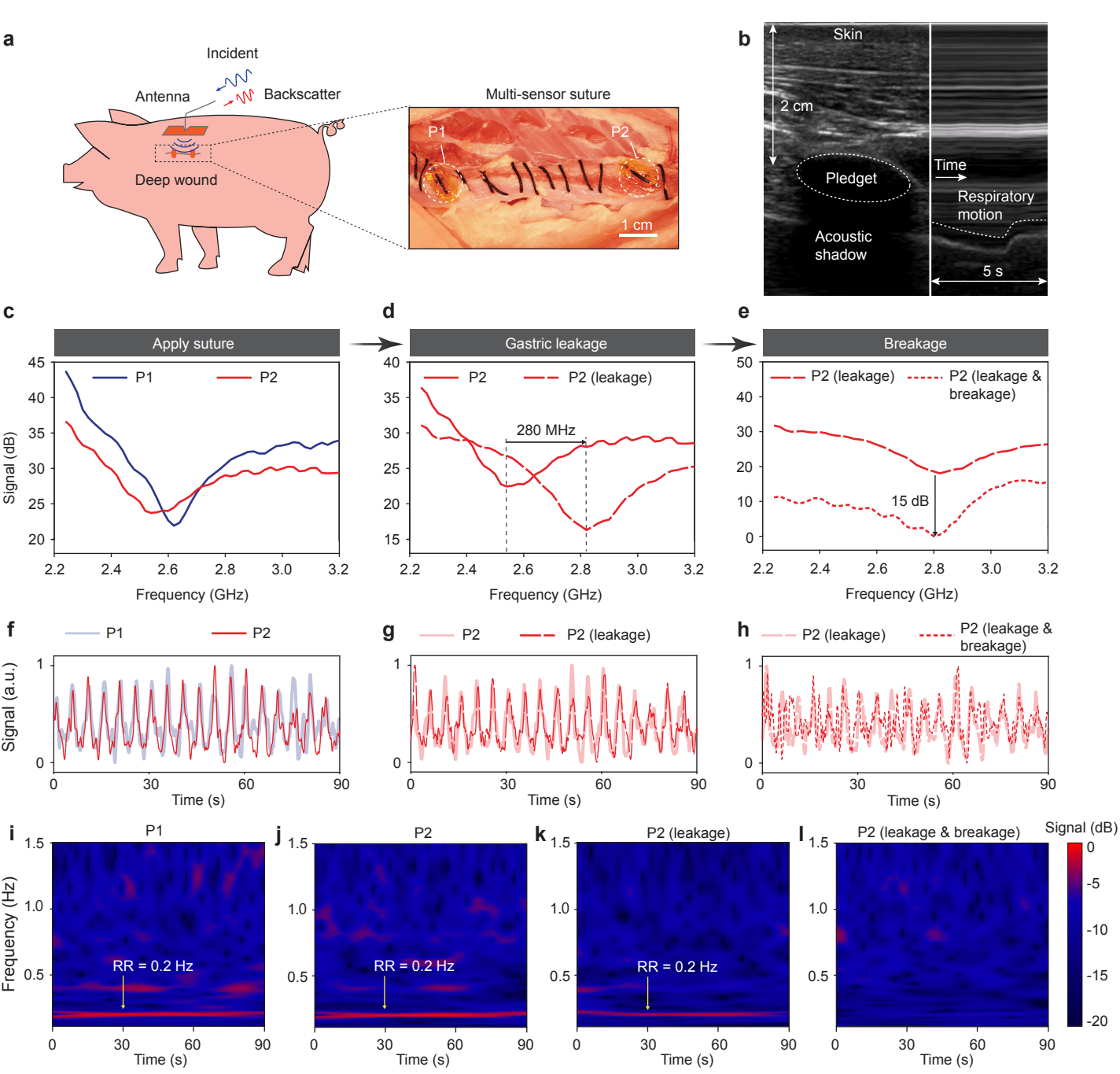
a
Incident
Antenna
Backscatter
Deep wound
Multi-sensor suture
P1
P2
1 cm
b
Skin
2 cm
Pledget
Acoustic shadow
Time
Respiratory motion
5 s
c
Apply suture
P1
P2
Signal (dB)
Frequency (GHz)
d
Gastric leakage
P2
P2 (leakage)
280 MHz
Frequency (GHz)
e
Breakage
P2 (leakage)
P2 (leakage & breakage)
15 dB
Frequency (GHz)
f
P1
P2
Signal (a.u.)
Time (s)
g
P2
P2 (leakage)
Time (s)
h
P2 (leakage)
P2 (leakage & breakage)
Time (s)
i
P1
Frequency (Hz)
RR = 0.2 Hz
Time (s)
j
P2
RR = 0.2 Hz
Time (s)
k
P2 (leakage)
RR = 0.2 Hz
Time (s)
l
P2 (leakage & breakage)
Time (s)
Signal (dB)

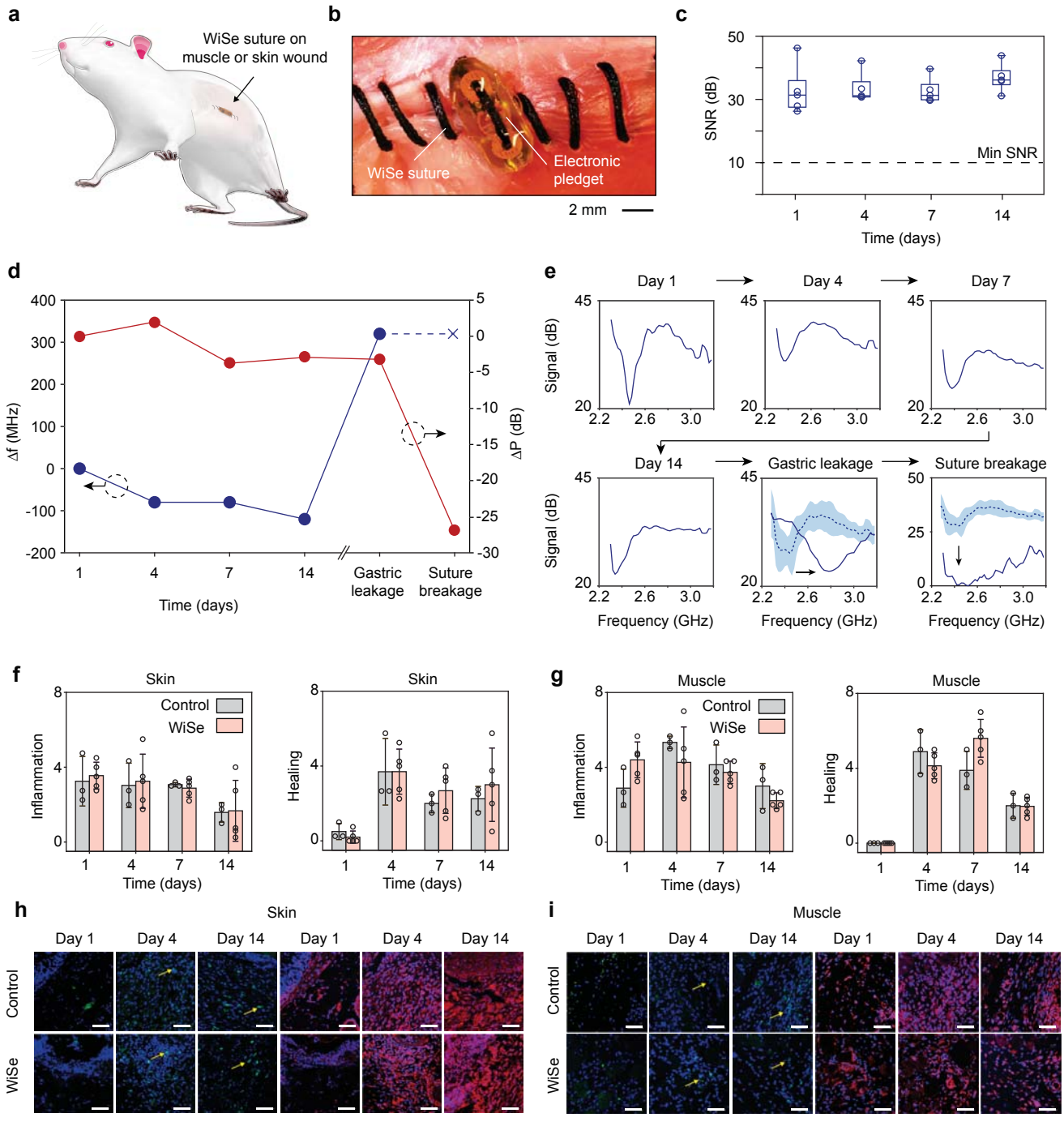
a
WiSe suture on
muscle or skin wound
b
WiSe suture
Electronic
pledget
2 mm
c
SNR (dB)
Min SNR
Time (days)
d
Δf (MHz)
ΔP (dB)
Gastric
leakage
Suture
breakage
Time (days)
e
Day 1
Day 4
Day 7
Day 14
Gastric leakage
Suture breakage
Signal (dB)
Frequency (GHz)
f
Skin
Control
WiSe
Inflammation
Healing
Time (days)
g
Muscle
h
Skin
i
Muscle
Day 1
Day 4
Day 14
Control
WiSe

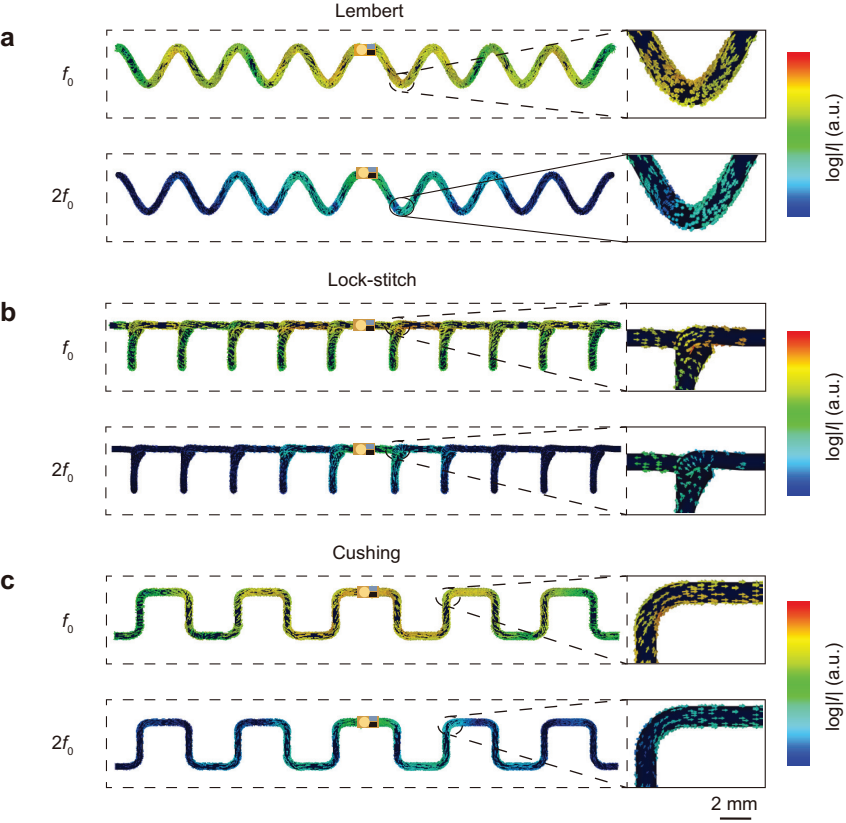
a
Lembert
f_0
$2f_0$
log|I| (a.u.)
b
Lock-stitch
f_0
$2f_0$
log|I| (a.u.)
c
Cushing
f_0
$2f_0$
log|I| (a.u.)
2 mm

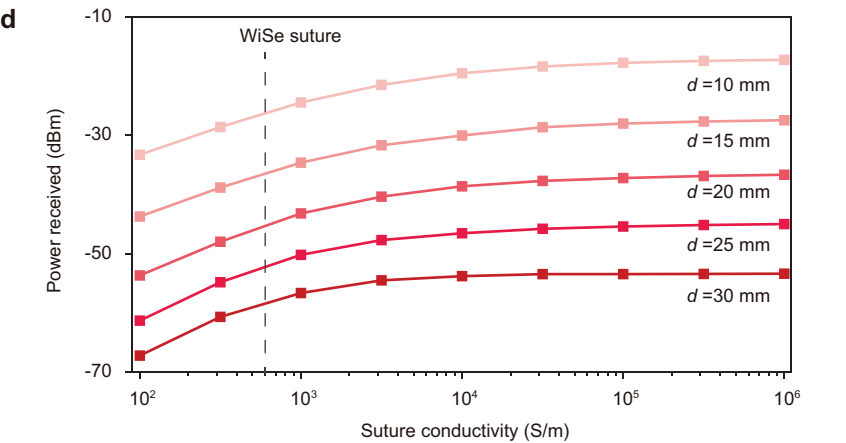
d
WiSe suture
d =10 mm
d =15 mm
d =20 mm
d =25 mm
d =30 mm
Power received (dBm)
-10
-30
-50
-70
10^2
10^3
10^4
10^5
10^6
Suture conductivity (S/m)

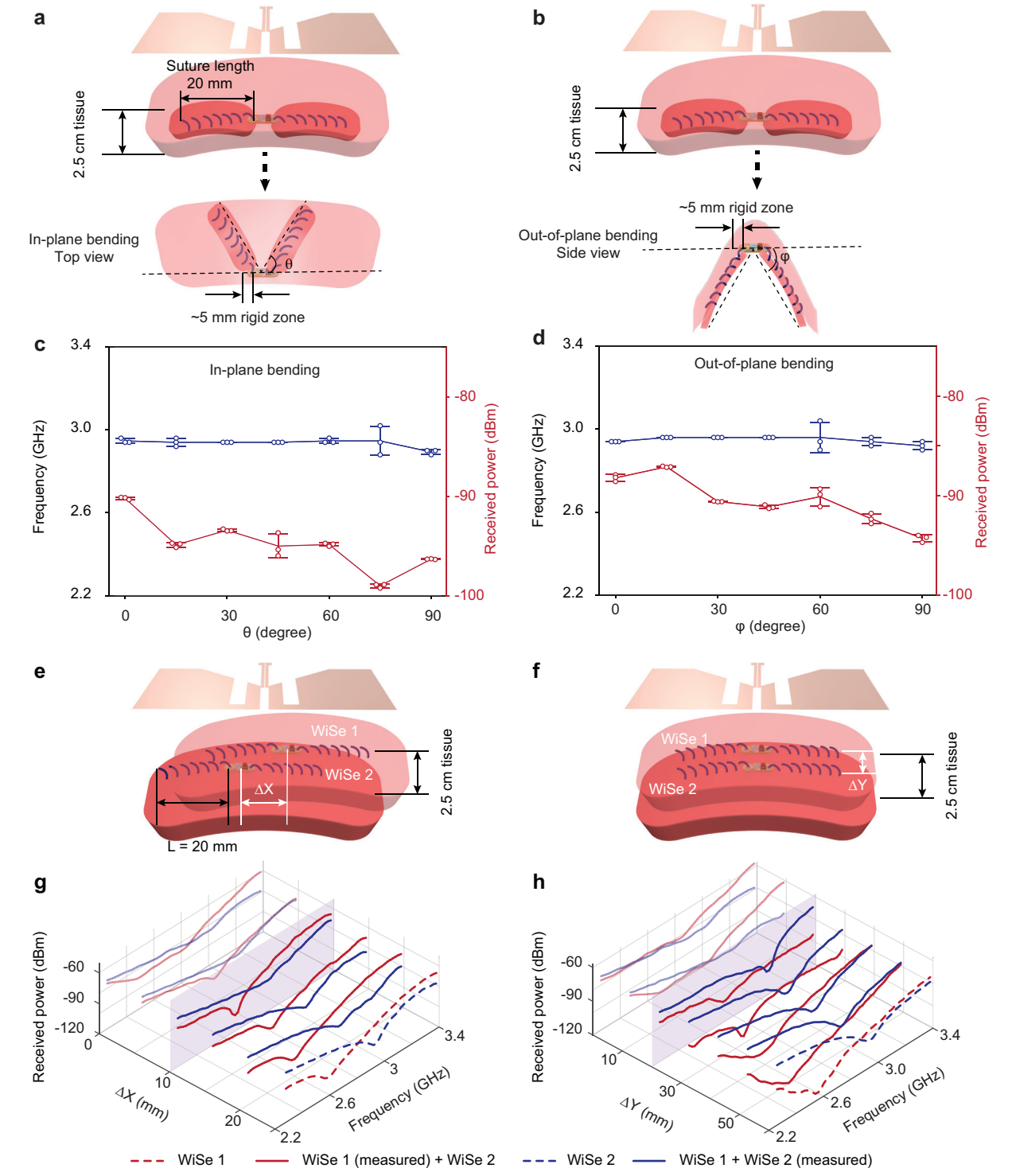
a
Suture length
20 mm
2.5 cm tissue
In-plane bending
Top view
θ
~5 mm rigid zone
b
2.5 cm tissue
~5 mm rigid zone
Out-of-plane bending
Side view
φ
c
In-plane bending
Frequency (GHz)
Received power (dBm)
θ (degree)
d
Out-of-plane bending
Frequency (GHz)
Received power (dBm)
φ (degree)
e
WiSe 1
WiSe 2
ΔX
2.5 cm tissue
L = 20 mm
f
WiSe 1
WiSe 2
ΔY
2.5 cm tissue
g
Received power (dBm)
ΔX (mm)
Frequency (GHz)
h
Received power (dBm)
ΔY (mm)
Frequency (GHz)
WiSe 1
WiSe 1 (measured) + WiSe 2
WiSe 2
WiSe 1 + WiSe 2 (measured)

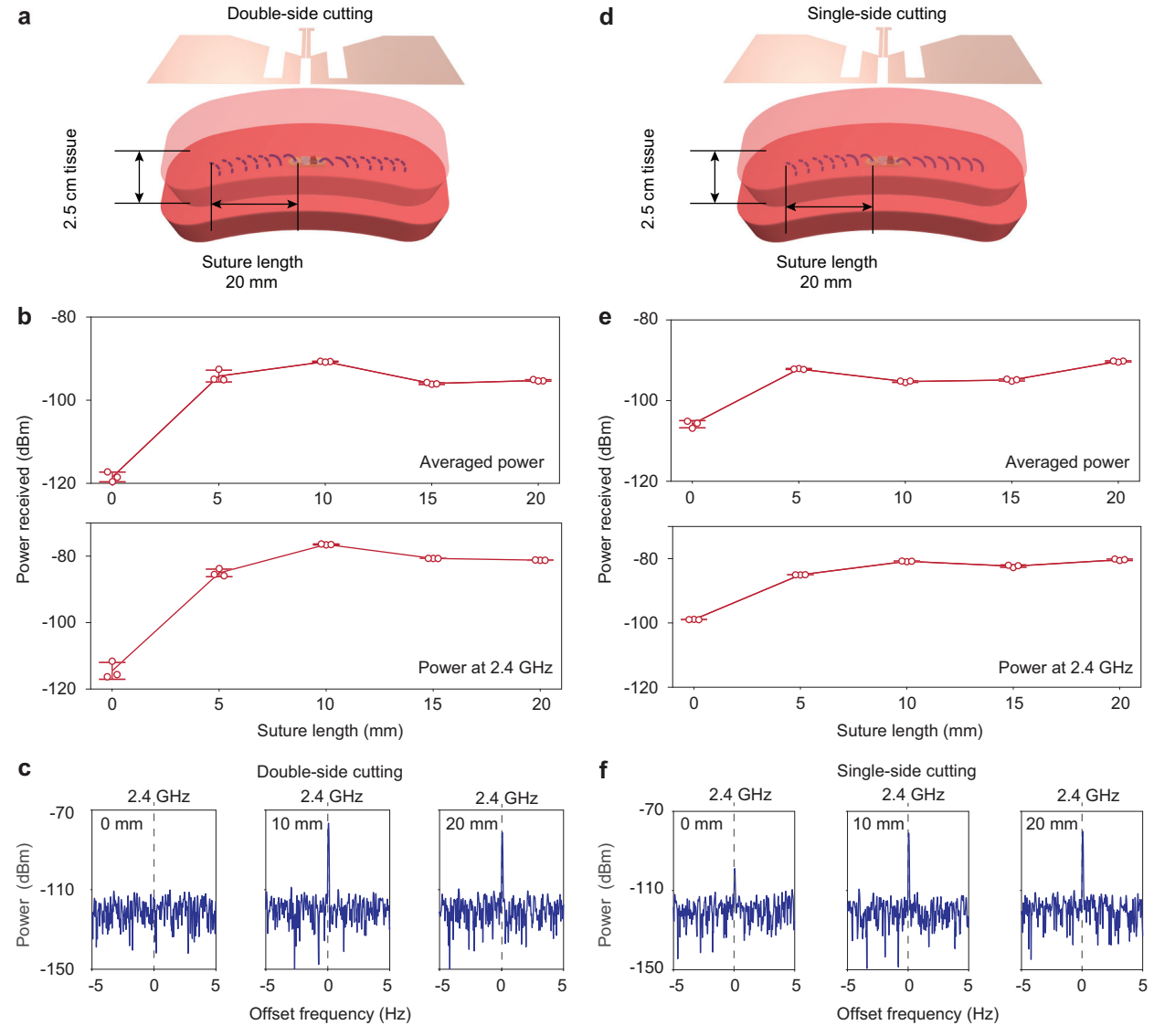
a
Double-side cutting
2.5 cm tissue
Suture length
20 mm
d
Single-side cutting
2.5 cm tissue
Suture length
20 mm
b
Power received (dBm)
-80
-100
-120
Averaged power
0
5
10
15
20
-80
-100
-120
Power at 2.4 GHz
Suture length (mm)
e
Power received (dBm)
-80
-100
-120
Averaged power
0
5
10
15
20
-80
-100
-120
Power at 2.4 GHz
Suture length (mm)
c
Double-side cutting
2.4 GHz
0 mm
2.4 GHz
10 mm
2.4 GHz
20 mm
Power (dBm)
-70
-110
-150
-5
0
5
Offset frequency (Hz)
f
Single-side cutting
2.4 GHz
0 mm
2.4 GHz
10 mm
2.4 GHz
20 mm
Power (dBm)
-70
-110
-150
-5
0
5
Offset frequency (Hz)

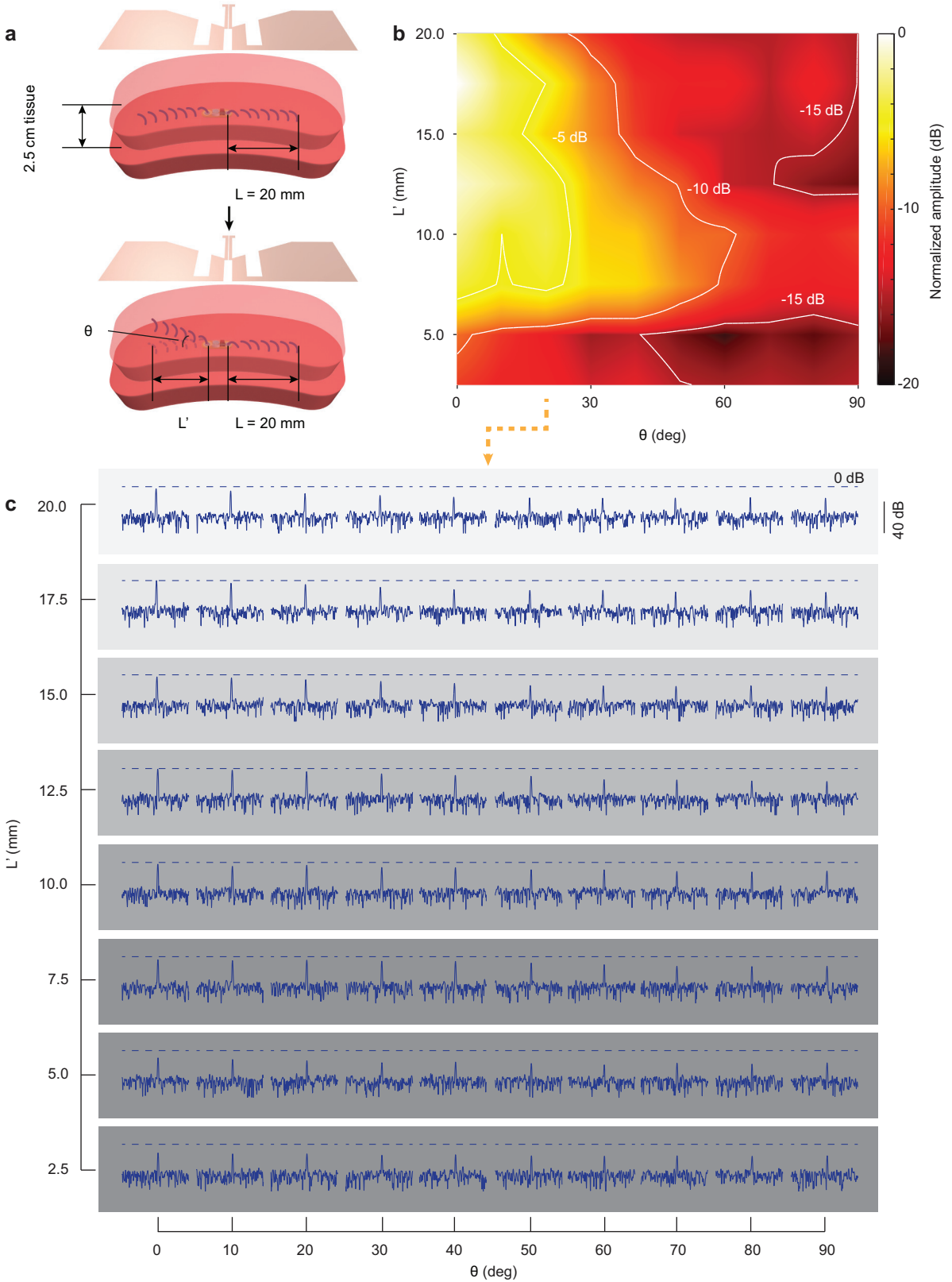
a
2.5 cm tissue
L = 20 mm
θ
L'
L = 20 mm
b
L' (mm)
20.0
15.0
10.0
5.0
-5 dB
-10 dB
-15 dB
-15 dB
0
30
60
90
θ (deg)
0
-10
-20
Normalized amplitude (dB)
c
0 dB
40 dB
L' (mm)
20.0
17.5
15.0
12.5
10.0
7.5
5.0
2.5
0
10
20
30
40
50
60
70
80
90
θ (deg)

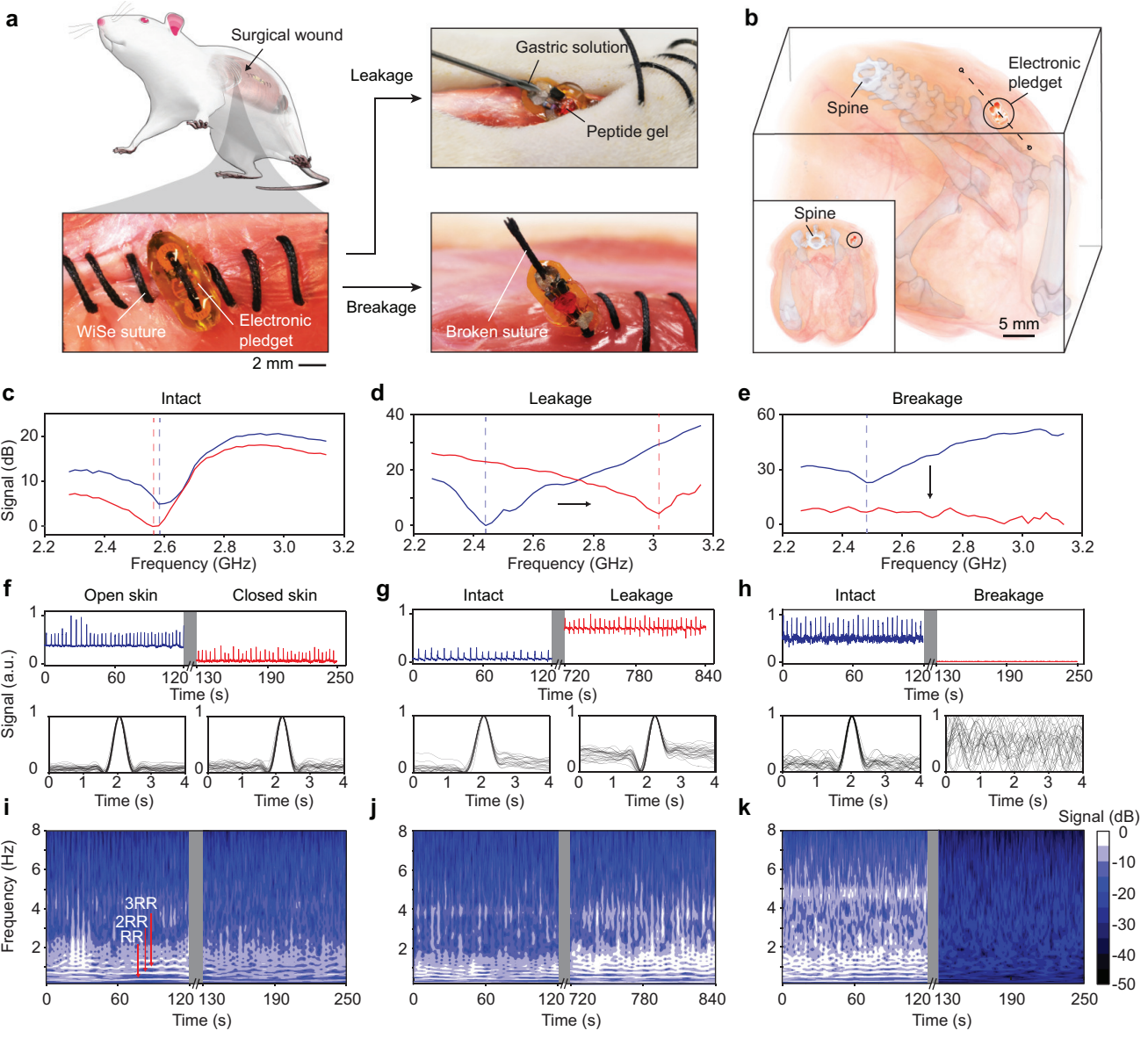
a
Surgical wound
Leakage
Gastric solution
Peptide gel
Breakage
Broken suture
WiSe suture
Electronic pledget
2 mm
b
Spine
Electronic pledget
Spine
5 mm
c
Intact
Signal (dB)
Frequency (GHz)
d
Leakage
Frequency (GHz)
e
Breakage
Frequency (GHz)
f
Open skin
Closed skin
Signal (a.u.)
Time (s)
g
Intact
Leakage
Time (s)
h
Intact
Breakage
Time (s)
i
Frequency (Hz)
3RR
2RR
RR
Time (s)
j
Time (s)
k
Signal (dB)
Time (s)

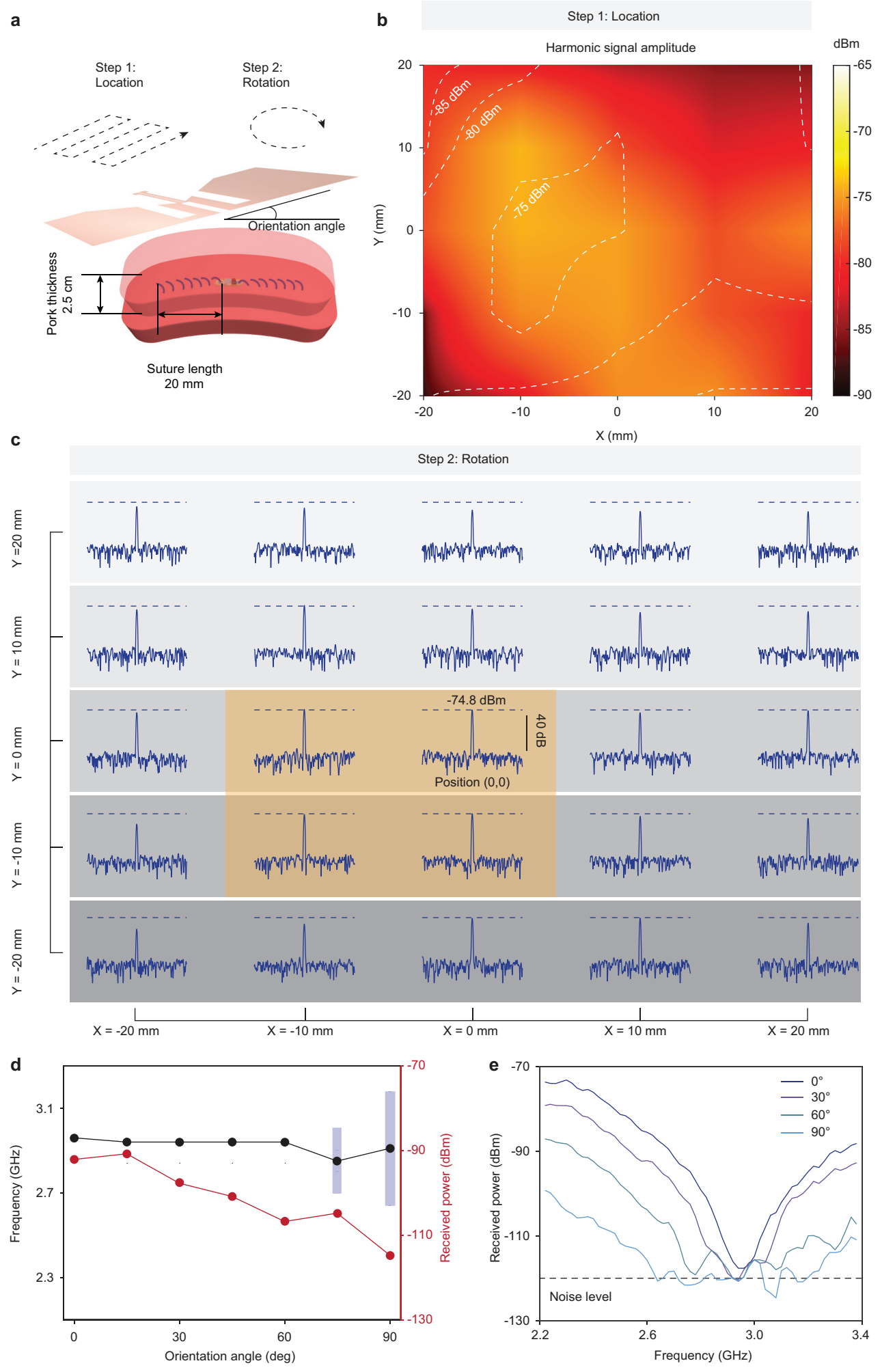
a
Step 1:
Location
Step 2:
Rotation
Orientation angle
Pork thickness
2.5 cm
Suture length
20 mm
b
Step 1: Location
Harmonic signal amplitude
dBm
-65
-70
-75
-80
-85
-90
-85 dBm
-80 dBm
-75 dBm
Y (mm)
X (mm)
20
10
0
-10
-20
c
Step 2: Rotation
Y =20 mm
Y = 10 mm
Y = 0 mm
Y = -10 mm
Y = -20 mm
-74.8 dBm
40 dB
Position (0,0)
X = -20 mm
X = -10 mm
X = 0 mm
X = 10 mm
X = 20 mm
d
Frequency (GHz)
3.1
2.7
2.3
-70
-90
-110
-130
Received power (dBm)
0
30
60
90
Orientation angle (deg)
e
Received power (dBm)
-70
-90
-110
-130
0°
30°
60°
90°
Noise level
2.2
2.6
3.0
3.4
Frequency (GHz)

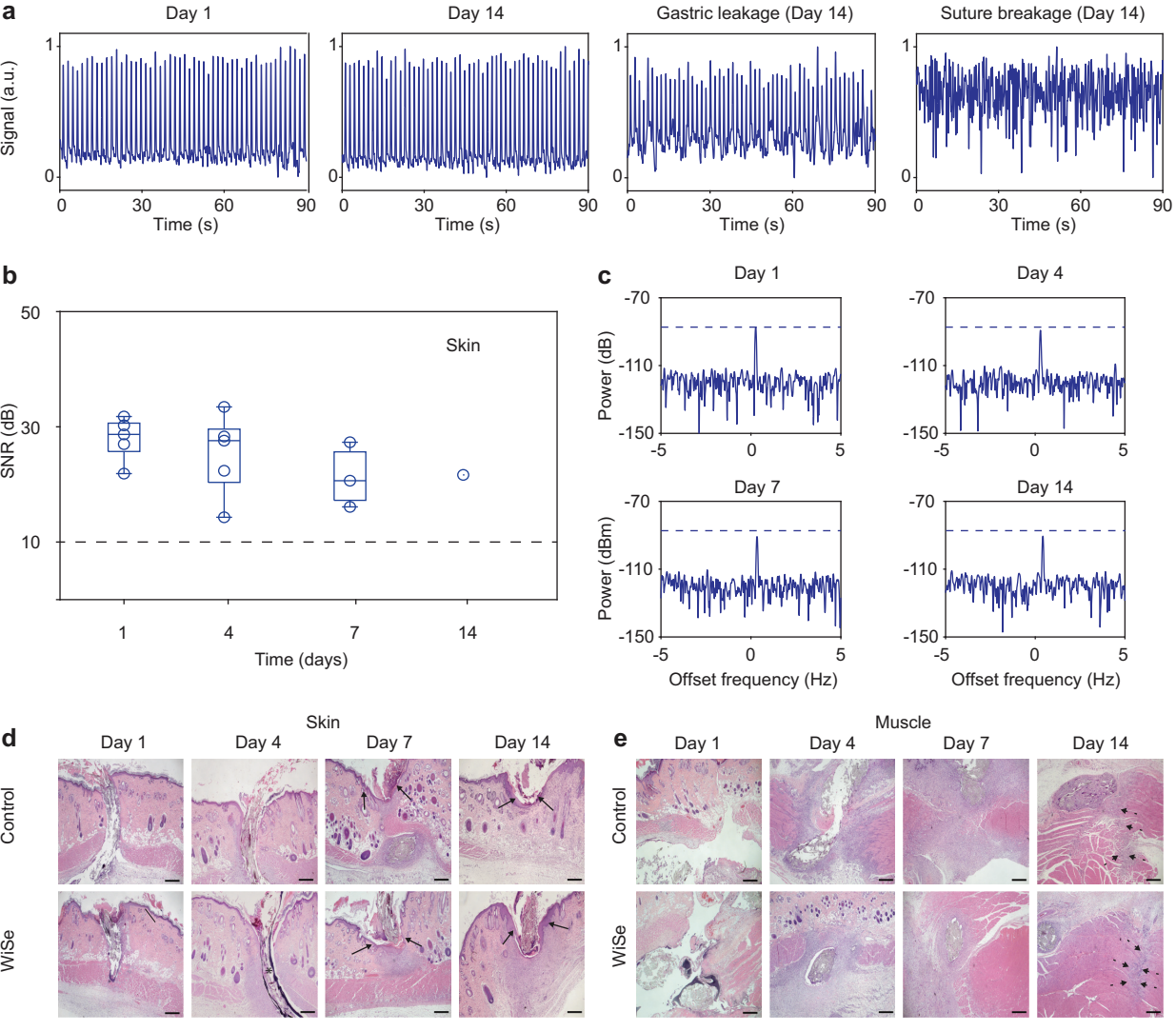
a
Day 1
Day 14
Gastric leakage (Day 14)
Suture breakage (Day 14)
Signal (a.u.)
Time (s)
b
Skin
SNR (dB)
Time (days)
c
Day 1
Day 4
Day 7
Day 14
Power (dB)
Power (dBm)
Offset frequency (Hz)
d
Skin
Control
WiSe
e
Muscle

	Filename *ED_FIG#.ext* *ext can be jpg, tiff or eps*	**Figure title** *One sentence only*	**Figure caption**
ED Fig. 1	ED_FIG1.eps	**Radiofrequency response of different stitches and varying suture conductivity**	**Extended Data Fig. 1 | Radio-frequency response of different stitches and varying suture conductivity. a-c**, Current distribution on (**a**) Lembert, (**b**) lock, (**c**) Cushing stitches at the fundamental f_0 and harmonic $2f_0$ frequencies. The stitches are excited by a plane wave. **d**, Simulated received power detected by the wireless system at the second harmonic for Cushing stitch with varying conductivity at distance *d* from the antenna.
ED Fig. 2	ED_FIG2.eps	**Effect of tissue curvature and spacing between adjacent sutures**	**Extended Data Fig. 2 | Effect of tissue curvature and spacing between adjacent sutures. a, b,** Schematic of the experimental setup for in-plane bending (**a**) and out-of-plane bending (**b**). **c, d,** Resonant frequency and averaged power over the operational band (2.2–3.4 GHz) measured for varying in-plane (**c**) and out-of-plane (**d**) bending angles. Error bars show the mean ± s.d. (*n* = 3 samples). **e, f,** Schematic diagrams of the test setup for wireless interference of WiSe with different spacing in X direction (**e**) and Y direction (**f**). WiSe sutures are separately labelled as WiSe1 and WiSe2. **g, h,** Measured harmonic backscattering spectra with various spacing in X direction (**g**) and Y direction (**h**).
ED Fig. 3	ED_FIG3.eps	**Effect of suture length**	**Extended Data Fig. 3 | Effect of suture length. a,d** Schematic of the experimental setup for suture with double-side (**a**) or single-side (**c**) cutting. The suture is placed under 2.5 cm porcine tissue and the length of varied Lembert stitches. **b,e** Averaged received power and received harmonic power (at 2.4 GHz) of WiSe over the operation band with double-side (**b**) or single-side (**d**) cutting. Error bars show the mean ± s.d. (*n* = 3 samples). **c,f** Harmonic signal received (at 2.4 GHz) for sutures with length 0, 10, and 20 mm on each side (**c**) or left side (**e**) of the pledget.

ED Fig. 4	ED_FIG4.eps	**WiSe suture breakage test**	**Extended Data Fig. 4 | WiSe suture breakage test. a,** Schematic of test setup for simulating suture breakage under 2.5 cm porcine tissue. **b,** Heatmap of the received harmonic signal power as a function of the length of the left segment of the suture and the angle θ of the unravelled segment. **c,** Corresponding measured harmonic signal at 2.4 GHz. The signals are normalized to the initial suture state (0 dB). The angle θ is used to vary the effective length of the dipole antenna formed by the suture. In clinical applications, the unravelled segment is expected to spontaneously bunch together due to agitation by natural body motions[61], which also leads to reduction of the effective dipole antenna length.
ED Fig. 5	ED_FIG5.eps	***In vivo* post-operative monitoring in a rat model**	**Extended Data Fig. 5 | *In vivo* post-operative monitoring in rat model. a**, Illustration of the rodent surgical wound model. WiSe sutures were used to close an incision on the gluteal muscle and the skin over the wound stitched with unmodified silk sutures. Leakage of gastric fluid is simulated by subcutaneous injection of artificial gastric solution and breakage of the suture by cutting near the center of the surgical stitch. **b**, Computed tomography image of the surgical site. Dashed lines show WiSe suture estimated from the position of electronic pledget. **c-e**, Frequency-resolved wireless readout of the WiSe suture during implantation (**c**), gastric leakage (**d**), and suture breakage (**e**). Signal amplitudes were separately normalized based on the minimum amplitude of each group. **f-h**, Time-resolved wireless readout of the WiSe suture during implantation (**f**), gastric leakage (**g**), and suture breakage (**h**). Lower panels show respiratory waveforms aligned and normalized to the peak. **i**-**k**, Spectrogram (continuous wavelet transform) of the time-resolved signal. Red arrows indicate spectral peaks corresponding to the respiratory rate (RR, 0.28 Hz) and its second and third harmonics.

ED Fig. 6	ED_FIG6.eps	**Reader antenna positioning**	**Extended Data Fig. 6 | Reader antenna positioning. a,** Illustration of the steps to position the reader antenna. **b,** Contour plot of the received harmonic signal power when the position of the antenna is scanned within a 40 mm × 40 mm area. **c,** Measured backscattering signal for the antenna positions in (**b**). Yellow shading indicates the 10 mm × 10 mm area with highest signal amplitude. **d**, Resonant frequency and received power as a function of the orientation angle of the antenna. Blue shading denotes the frequency uncertainty due to decrease in the signal-to-noise ratio. **e,** Harmonic backscattering spectra for varying orientation angles.
ED Fig. 7	ED_FIG7.eps	**Chronic wireless sensing *in vivo***	**Extended Data Fig. 7 | Chronic wireless sensing *in vivo*. a,** Time-resolved wireless readout of WiSe suture applied to muscle wound on day 1, day 14, after simulated gastric leakage on day 14, and after simulated suture breakage on day 14. **b,** Signal-to-noise ratio (SNR) of wireless readout from WiSe sutures applied to skin wounds on rats over 14 days. Sutures are naturally removed by the rats as the skin wound heals. Box plots show the mean, upper quartile, and lower quartile (n = 5 rats on day 1 and n = 1 rat on day 14). **c,** Backscattering signals from a WiSe suture applied to a muscle wound over 14 days. Dash line indicates the harmonic signal amplitude on day 1. **d**, **e**, Representative H&E-stained tissue sections from the skin and muscle wounds near the sutures. Solid black arrows show skin re-epithelization (**d**), dashed black arrows show wound closure in muscle (**e**). Scale bars, 500 μm.

	Filename	**A brief description of the contents** *Example: Supplementary methods, discussion, figures, tables, references and video captions.*
Main Supplementary Information	SI.pdf	**Supplementary notes, figures, tables, references and video captions.**
Reporting Summary	RS.pdf	

Type *type must be one of these options: data, table, video, audio, code*	**Filename** *AS_YYY#.ext* *ext can be pdf, jpg, tiff, xlsx, mp3, mp4, mov, txt, zip*	**A brief description of the contents** *These have to be short yet specific (typically, a single sentence).* *Full descriptions can be listed at the end of the main SI.*
video	AS_VID1.mp4	Suturing technique by threading the electronic pledget.
video	AS_VID2.mp4	Suturing technique by knotting the electronic pledget.
video	AS_VID3.mp4	Real-time wireless response of a surgical stitch.
video	AS_VID4.mp4	Frequency-resolved wireless readout of a deep surgical stitch.
video	AS_VID5.mp4	Ultrasound imaging of a suture in a porcine model.

4
5

	Filename *SD_[ED_]YYY#.ext* *ext can be txt, xlsx, jpg, tiff or pdf.*	**A brief description of the content** *Examples: Source data, Source data and statistics, Statistics, Unprocessed Western blots, Unprocessed gels.*
SD for Fig. 5	SD_FIG5.xlsx	Source data for panels f and g.